

LEBANESE AMERICAN UNIVERSITY

Multiple Site-Specific Analyses of the Stability of Quarried Slopes in
Lebanon Based on Unmanned Aerial Vehicle Photogrammetry

By

Saad Allah Imad Solh

A thesis

Submitted in Partial Fulfillment of the requirements

for the degree of Master of Science in Civil and Environmental Engineering

School of Engineering

April 2022

© 2022

Saad Allah Imad Solh

All Rights Reserved

THESIS APPROVAL FORM

Student Name: **Saad Allah Solh** I.D. #: **201408954**

Thesis Title : **Multiple Site-Specific Analyses of the Stability of Quarried Slopes in Lebanon Based on Unmanned Aerial Vehicle Photogrammetry**

Program: **M.S. in Civil & Environmental Engineering**

Department: **Civil Engineering**

School: **Engineering**

The undersigned certify that they have examined the final electronic copy of this thesis and approved it in Partial Fulfillment of the requirements for the degree of:

Masters in the major of **Civil Engineering**

| | | | |
|---|-----------|---|--|
| Thesis Advisor's Name Dr. Grace Abou Jaoude | Signature |  | DATE: 10 / 05 / 2022 <small>Day Month Year</small> |
| Committee Member's Name Dr. Caesar Abi Shdid | Signature |  | DATE: 10 / 05 / 2022 <small>Day Month Year</small> |
| Committee Member's Name Dr. Moustapha Harb | Signature |  | DATE: 10 / 05 / 2022 <small>Day Month Year</small> |

THESIS COPYRIGHT RELEASE FORM

LEBANESE AMERICAN UNIVERSITY NON-EXCLUSIVE DISTRIBUTION LICENSE

By signing and submitting this license, you (the author(s) or copyright owner) grants the Lebanese American University (LAU) the non-exclusive right to reproduce, translate (as defined below), and/or distribute your submission (including the abstract) worldwide in print and electronic formats and in any medium, including but not limited to audio or video. You agree that LAU may, without changing the content, translate the submission to any medium or format for the purpose of preservation. You also agree that LAU may keep more than one copy of this submission for purposes of security, backup and preservation. You represent that the submission is your original work, and that you have the right to grant the rights contained in this license. You also represent that your submission does not, to the best of your knowledge, infringe upon anyone's copyright. If the submission contains material for which you do not hold copyright, you represent that you have obtained the unrestricted permission of the copyright owner to grant LAU the rights required by this license, and that such third-party owned material is clearly identified and acknowledged within the text or content of the submission. IF THE SUBMISSION IS BASED UPON WORK THAT HAS BEEN SPONSORED OR SUPPORTED BY AN AGENCY OR ORGANIZATION OTHER THAN LAU, YOU REPRESENT THAT YOU HAVE FULFILLED ANY RIGHT OF REVIEW OR OTHER OBLIGATIONS REQUIRED BY SUCH CONTRACT OR AGREEMENT. LAU will clearly identify your name(s) as the author(s) or owner(s) of the submission, and will not make any alteration, other than as allowed by this license, to your submission.

Name: Saad Allah Imad Solh

Signature:



Date: 10 / 05 /2022

Day Month Year

PLAGIARISM POLICY COMPLIANCE STATEMENT

I certify that:

1. I have read and understood LAU's Plagiarism Policy.
2. I understand that failure to comply with this Policy can lead to academic and disciplinary actions against me.
3. This work is substantially my own, and to the extent that any part of this work is not my own I have indicated that by acknowledging its sources.

Name: Saad Allah Imad Solh

Signature:

[Redacted Signature]

Date: 10 / 05 /2022

Day Month Year

To my beloved parents, Imad and Nazeck, who have always been my source of inspiration and strength when I thought of giving up, and who continually provide their moral, spiritual, emotional, and financial support

To my brother, sisters, relatives, and friends who shared their words of advice and encouragement to finish this study

I dedicate my humble work.

ACKNOWLEDGMENT

I would like to express my sincere gratitude to my advisor, Dr. Grace Abou Jaoude, for her invaluable assistance and insights leading to the writing of this thesis. Thank you to my committee members, Dr. Caesar Abi Shdid and Dr. Moustapha Harb. Your encouraging words and thoughtful, detailed feedback have been very important to me.

I would also like to thank Mrs. Rouba Kaafarani, my colleague, for her great feedback, excellent encouragement, and guidance. Thank you to my sister, Ghida Solh, for always being there for me and for helping me throughout all my site visits

Most importantly, I am grateful for my family's unconditional, unequivocal, and loving support.

Multiple Site-Specific Analyses of the Stability of Quarried Slopes in Lebanon Based on Unmanned Aerial Vehicle Photogrammetry

Saad Allah Solh

ABSTRACT

Landslide hazards associated with the quarrying sector in Lebanon are a source of public concern due to the adverse environmental and social impacts imposed by illegal quarrying activities. Such activities have been leading to direct threats to human lives and property damage. Regional landslide hazard and risk maps have been developed based on a multi-model analysis performed through the framework of a Geographic Information System (GIS) software using a 15-meter digital elevation model (DEM) by Grant et al. (2016) and Pollock et al. (2019) and their accuracy was validated for natural terrain. The use of these maps for stability assessment of quarry locations was examined by Kaafarani (2020) and was found to be limited because of the steepness of these man-made slopes and the inability of the 15-meter DEM to capture the real topography. The aim of this work is to determine, from multiple site-specific analyses, the most probable mode(s) of failure of such steep rock slopes and to assess the extent to which a failure may impact the surrounding urbanized zones. Remote sensing using Unmanned Aerial Vehicle (UAV) photogrammetry was used to map four limestone quarries located in the Anti-Lebanon Mountain Range. The stability of the studied quarries controlled by geometry and strength of the discontinuities was first evaluated kinematically and then analysed using limit equilibrium methods under dry, rainfall, and seismic conditions. The overall stability of the quarries was also assessed based on the geological strength index (GSI) classification and the rock mass geomechanical properties were based on the generalized Hoek- Brown constants. Risk of block failure along discontinuities was observed and wedge sliding, in particular, had the highest probability of occurrence. The maximum runout distance obtained was less than 9 meters in all sites. The results did not show risk of general failure in any of the four quarries. The outcome of this study can be used to update the regional-scale maps by refining the analysis in quarry locations, to develop strict regulations for future quarrying operations, and to implement a mitigation plan that protected further urbanization projects in areas near dormant and abandoned quarry sites.

Keywords: Quarrying – Rock slope – Landslide – Regional scale – DEM – UAV – Remote sensing - Rock mass classification – Kinematic analysis – Limit equilibrium method – Runout Distance

TABLE OF CONTENTS

| Chapter | Page |
|--|-----------|
| Chapter One Introduction..... | 1 |
| 1.1 General | 1 |
| 1.2 Description of Selected Quarry Sites | 7 |
| Chapter Two Literature Review..... | 9 |
| 2.1 Geology, Climate, and Tectonic setting of Lebanon | 9 |
| 2.2 Failures of Quarry Slopes | 10 |
| 2.2.1 Cases of Quarry Failures Worldwide..... | 11 |
| 2.2.2 Cases of Quarry Failures in Lebanon | 12 |
| 2.3 Rock Mechanics Overview | 13 |
| 2.3.1 Rock Mass and Intact Rock | 13 |
| 2.3.2 Orientation of Discontinuities..... | 17 |
| 2.3.3 Stereographic Projections | 18 |
| 2.4 Discontinuities Mapping Techniques | 20 |
| 2.4.1 Traditional Mapping Technique | 20 |
| 2.4.2 Remote Sensing Techniques | 21 |
| 2.5 Rock Slope Failure Mechanisms | 23 |
| 2.5.1 Structurally Controlled Failure | 24 |
| 2.5.2 Non-Structurally Controlled Failure | 28 |
| 2.6 Example of Slope Stability Analysis based on Structurally Controlled Failure | |
| 30 | |
| Chapter Three Methodology..... | 33 |
| 3.1 Different Software Used in this Research | 34 |
| 3.2 Definition of Parameters Used | 35 |
| 3.3 UAV-based Remote Sensing Survey | 37 |

| | |
|---|-----------|
| 3.4 Semi-Automated Discontinuity Extraction | 42 |
| 3.5 Estimation of the Strength Parameters Along the Discontinuities | 44 |
| 3.6 Estimation of the Strength Parameters of the Rock Mass | 45 |
| 3.7 Kinematic Analysis | 46 |
| 3.8 Analysis of Structurally Controlled Failures using Limit Equilibrium methods 47 | |
| 3.9 Analysis of Non- Structurally Controlled Failures using Limit Equilibrium methods | 48 |
| 3.10 Runout Distance and Angle of Reach | 49 |
| Chapter Four Interpretation of Results | 51 |
| 4.1 Digital Elevation Model (DEM) of the Four Quarries Mapped using UAV | 51 |
| 4.2 Discontinuity Orientation Extraction | 53 |
| 4.3 Kinematic Analysis of Quarry Faces..... | 55 |
| 4.3.1 Planar Failure | 55 |
| 4.3.2 Wedge Failure..... | 57 |
| 4.3.3 Toppling Failure | 60 |
| 4.4 Dominant Mode of Failure | 60 |
| 4.5 Stability Analysis of the Quarry Faces Based on Limit Equilibrium Methods | 62 |
| 4.5.1 RocPlane Results | 63 |
| 4.5.2 SWedge Results | 64 |
| 4.6 Stability Analysis Results for Non-Structurally Controlled Failure Based on Limit Equilibrium Methods..... | 66 |
| 4.7 Maximum Runout Distance and Angle of Reach..... | 68 |
| Chapter Five Conclusion and Limitations..... | 73 |
| References | 75 |

List of Tables

| | |
|---|----|
| Table 1: Sites Description | 36 |
| Table 2: Statistical parameters used in DSE (Riquelme et al. (2014))..... | 43 |
| Table 3: Barton-Bandis strength paramerts for the four quarries | 45 |
| Table 4: Hoek-Brown Parameters | 46 |
| Table 5: Summary of coefficient of restitution and friction coefficients used for rockfall analysis | 50 |
| Table 6: Discontinuity sets extracted from the point clouds..... | 53 |
| Table 7: Probability of failure modes for each quarry sites | 61 |
| Table 8: Total probability of the three failure modes | 62 |
| Table 9: Factors of safety determined from RocPlane under dry and wet conditions, as well as seismic loading..... | 63 |
| Table 10: Factors of safety determined from SWedge under dry and wet conditions, as well as seismic loading..... | 65 |
| Table 11: Factors of safety determined from Slide2 under dry and wet conditions, as well as seismic loading..... | 66 |
| Table 12: Runout Distance and Angle of Reach calculated using RocFall | 70 |

List of Figures

| | |
|--|----|
| Figure 1: Map showing the areas where the quarries should be located according to the National Master Plan for Quarries and the actual quarry locations in Lebanon (by Antoine Atallah)..... | 4 |
| Figure 2: Overlay quarry site map with slope map. Two examples of quarry sites 1) and 2) with a slope face angle of less than 35° based on 15-m DEM..... | 6 |
| Figure 3: Images by Google Earth of the quarry faces shown in Figure 2 | 6 |
| Figure 4: Locations of the study areas | 8 |
| Figure 5: Major geologic units and faults (bold) of Lebanon (Source: (Grant et al. 2016))..... | 10 |
| Figure 6: Quarry failure in a) Trabzon, Turkey and b) Waikari, New Zealand..... | 12 |
| Figure 7: Residential areas threatened by quarry near Nahr El Mott, North of Beirut | 13 |
| Figure 8: Hoek–Brown failure criterion..... | 15 |
| Figure 9: Joints: (a) filled and (b) unfilled | 16 |
| Figure 10: Roughness profiles and corresponding JRC values (After Barton and Choubey 1977)..... | 17 |
| Figure 11: Terminology defining discontinuity orientation: (a) isometric view of plane (dip and dip direction); (b) isometric view of line (plunge and trend)..... | 18 |
| Figure 12: Equal area projections of plane and line: (a) plane projected as great circle and corresponding pole; (b) line projected as pole (Source: Wyllie, 2015)..... | 19 |
| Figure 13: Polar and equatorial projections of a sphere..... | 19 |
| Figure 14: (a) A pole plot and (b) an isometric view of the three planes. | 20 |
| Figure 15: The two instruments used in remote sensing technology: a) TLS and b) SfM | 22 |

| | |
|---|----|
| Figure 16: Slope failure mechanisms: a) structurally controlled failure b) non-structurally controlled failure. Source: (Hudson & Harrison, 1997) | 24 |
| Figure 17: Planar sliding kinematic analysis | 25 |
| Figure 18: Wedge sliding kinematic analysis | 26 |
| Figure 19: Kinematic analysis toppling failure..... | 26 |
| Figure 20: Geological Strength Index Chart for Jointed Rocks..... | 29 |
| Figure 21: Methodology Flowchart | 34 |
| Figure 22: Contour maps of peak ground acceleration (PGA) with a 10% exceedance probability in 50 years (Huijer et al., 2011)..... | 36 |
| Figure 23: Level of Saturation (%) (Plassard, 1971) | 37 |
| Figure 24: UAV operation in Quarry 2 mapping..... | 38 |
| Figure 25: Image Acquisition Plan | 39 |
| Figure 26: Aarsal Quarry: a) Image by the DJI Phantom 4 Pro drone and b) 3D Model created using the SfM technique..... | 40 |
| Figure 27: Ain Bourday Quarry: a) Image by the DJI Phantom 4 Pro drone and b) 3D Model created using the SfM technique | 40 |
| Figure 28: Raiit Quarry: a) Image by the DJI Phantom 4 Pro drone and b) 3D Model created using the SfM technique..... | 41 |
| Figure 29: Janta Quarry: a) Image by the DJI Phantom 4 Pro drone and b) 3D Model created using the SfM technique..... | 41 |
| Figure 30: Critical Section of Quarry 3 clipped in CloudCompare | 42 |
| Figure 31: Overlaying DSE-detected joint sets on the quarry face in Quarry 1 using ClouCompare | 43 |
| Figure 32: GSI Selection for Quarry 1 based on Visual Comparison..... | 46 |
| Figure 33: Slope length and bench width..... | 48 |

| | |
|---|----|
| Figure 34: 2D cross-section extraction from 3D Model of Quarry 3..... | 49 |
| Figure 35: DEM of a) Quarry 1, b) Quarry 2, c) Quarry 3, and d) Quarry 4 | 52 |
| Figure 36: Satellite Image of the four quarry sites reproduced using Google Earth.. | 53 |
| Figure 37: The color scale represents the discontinuity sets assigned to each point of the critical face that was cropped from each quarry face. | 54 |
| Figure 38: The orientation of JS7 (from Quarry 3) obtained with b) DSE, was verified using a) ShapeMetrix software..... | 55 |
| Figure 39: JS2 in Quarry 4 shows a risk of planar sliding | 56 |
| Figure 40: Kinematic analysis of planar failure using DIPS on a) Quarry 1, b) Quarry 2, c) Quarry 3, and d) Quarry 4..... | 56 |
| Figure 41: Kinematic analysis of wedge failure using DIPS on a) Quarry 1, b) Quarry 2, c) Quarry 3, and d) Quarry 4..... | 57 |
| Figure 42: JS3 and JS8 showing a risk of wedge sliding (Quarry 1)..... | 58 |
| Figure 43: JS1 and JS4 showing a risk of wedge sliding (Quarry 2)..... | 58 |
| Figure 44: JS4 and JS7 showing a risk of wedge sliding (Quarry 3)..... | 59 |
| Figure 45: JS4 and JS7 showing a risk of wedge sliding (Quarry 4)..... | 59 |
| Figure 46: Kinematic analysis of flexural toppling using DIPS on a) Quarry 1, b) Quarry 2, c) Quarry 3, and d) Quarry 4 | 60 |
| Figure 47: Factor of safety of JS2 of Quarry 4 under (a) Dry conditions (b) Wet conditions (c) Seismic loading | 63 |
| Figure 48: 2D view of the JS2 model showing the applied and resultant forces under seismic event. | 64 |
| Figure 49: Factor of safety of wedge formed by JS1 and JS7 in Quarry 3 under (a) Dry conditions (b) Wet conditions (c) Seismic loading | 64 |

| | |
|---|----|
| Figure 50: Factor of safety of the overall slope in Quarry 1 under (a) Dry conditions (b) Wet conditions (c) Seismic loading..... | 67 |
| Figure 51: Overall Slope Stability Results for Quarry 2 under (a) Dry conditions (b) Wet conditions (c) Seismic loading | 67 |
| Figure 52: Overall Slope Stability Results for Quarry 3 under (a) Dry conditions (b) Wet conditions (c) Seismic loading | 68 |
| Figure 53: Overall Slope Stability Results for Quarry 4 under (a) Dry conditions (b) Wet conditions (c) Seismic loading | 68 |
| Figure 54: RocFall analysis of the wedge formed by JS3 & JS4 for Quarry 1..... | 69 |
| Figure 55: Distribution of rock fall path end locations of the wedge formed by JS3 & JS4 for Quarry 1..... | 70 |
| Figure 56: Rockfall Hazard shown in QGIS for a) Quarry 1, b) Quarry 2, c) Quarry 3, and d) Quarry 4 | 71 |
| Figure 57: Limestone Quarry Failure in New Zealand | 72 |
| Figure 58: Sketch showing the toe of slope and the parallel component of the weight | 74 |

Chapter One

Introduction

1.1 General

Rock slope instabilities often present major hazards and risks in mountainous regions causing significant economic losses, property damages, and human casualties especially near urban settlements and along transport corridors. (Froud & Petley, 2018; Pantelidis, 2009; Guzzetti et al., 1999). A hazard is defined as a process or situation with the potential to cause harm or other undesirable impacts. A risk is the chance, high or low, that any hazard will actually cause harm to someone or something. The level of risk thus results from the intersection of hazard with the value of the elements at risk by way of their vulnerability (Crozier & Glade, 2005). For landslides, the general concepts of hazard and risk described above apply equally: 'hazard' may be a large rockfall, 'likelihood' is the probability of its occurrence, and "risk" is the consequences depending on what will be affected by this rock break, the degree of damage it causes, and the costs incurred (Crozier & Glade, 2005).

Slope failures are triggered by several factors including rainfall, snowmelt, changes in water level, changes in groundwater, earthquakes, as well as human activities (Froud & Petley, 2018). For rainfall-induced landslides, the intensity and duration of the rainfall event play a major role in the stability of slopes (Rawat & Sharma, 2012). For instance, rockslides are caused by short outbursts of rain (Singh et al., 2016) while deep seated failures are caused by prolonged rainfall (Rahardjo et al., 1995). As for earthquake-induced landslides, they are controlled by the magnitude of the earthquake, the return period of the critical earthquake, and the site-specific ground acceleration that depends on the distance of the site from the epicenter and the focal depth

(Prakasam et al., 2021). In addition to these naturally induced landslide hazards, human activity also presents a significant factor that induces landslides (Froud & Petley, 2018). In practice, the record shows that the change caused by human land use is more detrimental to future landslide incidence than climate change (Anderson & Holcombe, 2013). For instance, people, especially in countries with lower gross national income (GNI) (Froud & Petley, 2018) tend to make near-vertical cuts while neglecting the design requirements that the angle of a safe cutting face must be compatible with the maximum allowable height (Wyllie, 2015). This is due to the fact that steep cuts are usually less expensive to construct because the volume of excavated rock is minimized, less acquisition of right-of-way is required, and smaller cut face areas are created (Wyllie, 2015). Over 700 deadly landslides that happened between 2004 and 2016 showed a human fingerprint, according to a study conducted by Froud and Petley (2018). The majority of human-induced landslides were caused by construction activities, legal and illegal mining, and unregulated hill cutting (Froud & Petley, 2018).

In the 1990's, Lebanon experienced rapid economic expansion and construction programs after 15 years of civil war which increased the demand for building materials such as stones, sand, and rocks to repair the damages of the conflict (El-Fadel et al., 2001). As a result, the country witnessed the exploitation of mountainous ecosystems for quarrying purposes and the formation of clearly visible scars over wide areas (Atallah et al., 2003). Darwish et al. (2008) presented the dangers of quarries in Lebanon, which included an increase in landslides and resulted in loss of natural ecosystems and biodiversity and a decrease of quantity and quality of water resources.

In 2002, the Lebanese government attempted to regulate land use planning and quarry operations. The Ministry of Environment drafted Decree No. 8803/2002 to regulate

the policies procedures for quarrying activities. The decree stipulated the possibility of establishing quarries in four regions: (1) Aarsal, (2) Tfail and Ain El Jaouz in Baalbek, (3) Yanta and Aita El Fokhar in Rachaiya and (4) Qousaya and Deir El Ghazal in Zahle, all of which are located in the Anti-Lebanon Mountain Range (MOE/UNDP/ECODIT, 2011). These areas form most of the border between Syria and Lebanon, cover about 163 km², and have a low population density. Nevertheless, the number of quarries and the areas they cover unfortunately increased from 784 quarries covering 2,897 ha in 1989 to 1278 quarries covering 5,267 ha in 2005, according to satellite images. In 2009, the Council of Ministers approved the National Master Plan for quarries updating the sites that are allowed to be invested in quarrying works, the methods of their operation, and the conditions for their rehabilitation after closure (MOE/UNDP/ECODIT, 2011). However, looking at the recent map (Figure 1) published by architect Antoine Atallah (2018) that is based on satellite images and not through direct field work, it is noticeable that the majority of the quarries are located outside the specific Lebanese territory that the government has deemed suitable for quarries. The minimal permit requests in the regions authorized by the National Master Plan for quarries are caused by two factors: first, the geographic distance of these areas from the coast, which raises the cost of transport and export compared to illegal quarries; second, corruption in state institutions and political favoritism that prevented the regulation of this sector (Public Works Studio, 2019). While most of the existing studies (Darwish et al., 2008; MOE/UNDP/ECODIT, 2011; Shaban et al., 2011) focus on the environmental impact of quarries on water and air resources, few have studied the stability of these high steep slopes (El-Fadel et al., 2001).

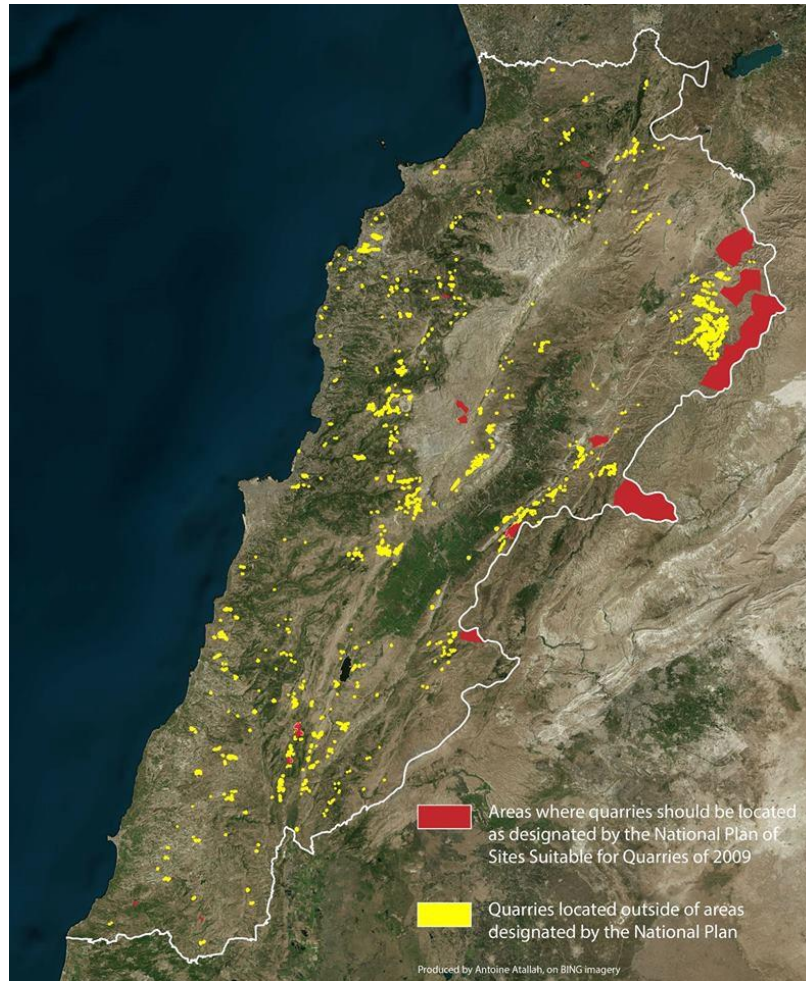


Figure 1: Map showing the areas where the quarries should be located according to the National Master Plan for Quarries and the actual quarry locations in Lebanon (by Antoine Atallah, 2018)

Grant et al. (2016) and Pollock et al. (2019) studied the stability of slopes under earthquake and rainfall events on the regional scale of the country. The two studies complement each other in generating landslide hazard and risk maps for the country. Their work was based on multimodal GIS approach in which the analysis was performed using the topographic slope extracted from the 15-m digital elevation map (DEM) and using the geologic units across Lebanon to assess the strength of the slopes. Slope inclination was adopted as an indicator to determine terrain susceptible to landslides: (1) slopes above 35° were assessed against rock-slope failures (2) slopes from 15° to 35° were assessed against coherent rotational failures and (3) slopes shallower than 15° were not considered likely to fail in any landslide mode. These

maps enhance risk communication that improves the public risk awareness and mitigation. Decision makers as well as laypeople, who may be affected by natural or man-made hazards, must understand the hazard itself, its impact, and the potential of protecting themselves from a disaster (Dransch et al., 2010).

The result of the work was validated through field visits to assess the zones where hazard and risk were identified. Given the coarseness of the DEM used in the work, man-made steep slopes could not be identified unlike naturally occurring slopes. Hence, the question was raised as to whether the outcome produced by Grant et al. (2016) and Pollock et al. (2019) could be useful for risk assessment at quarry sites.

A quick assessment was performed using QGIS by superimposing the slope angle map (based on the 15-m DEM) over the quarry sites map (Atallah, 2018). It was found that more than 90% of the quarries were not captured properly and that their slope angles were less than 35° . Thus, almost all “rock” quarries had been evaluated as coherent rotational failures. Figure 2 shows an example of two quarries with an angle of inclination of less than 35° according to the 15-m DEM, but when these sites were examined in Google Earth, it was clear that these slopes are quite steep, as shown in Figure 3. For the reasons mentioned above, and given that most quarries in Lebanon have steep faces exceeding 45° (El-Fadel et al., 2001), these regional-scale maps are less reliable for use in quarrying risk assessment. This simple exercise shows that the hazard and risk predictions for quarry sites must be improved and updated based on site-specific analysis with a more accurate and refined digital elevation map.

Kaafarani (2020) presented a methodology to assess the stability of quarried slopes under three conditions: dry condition, heavy rainfall condition, and seismic condition. In her work, she mapped a limestone quarry in Bafliye, South of Lebanon with a DJI

Phantom 4 V2.0 drone, recreated it as a 3D scene, assessed it kinematically, and then analysed the stability of its slope face using limit equilibrium and numerical modelling techniques. The results showed that this quarry is unstable under both seismic and rainfall events with a maximum runout distance of 7.76 m.

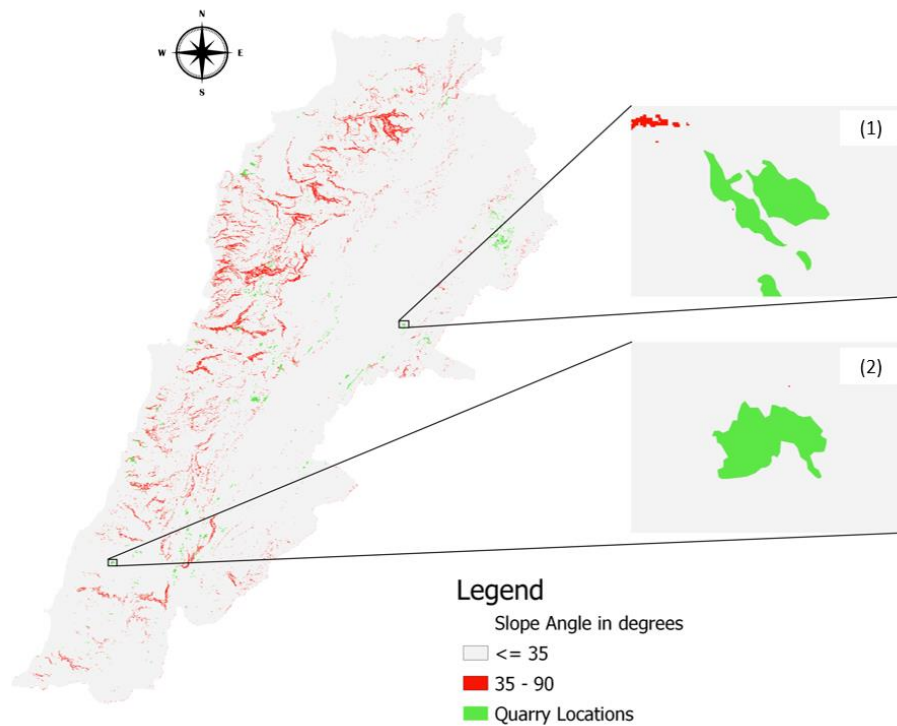


Figure 2: Overlay quarry site map with slope map. Two examples of quarry sites (1) and (2) with a slope face angle of less than 35° based on 15-m DEM

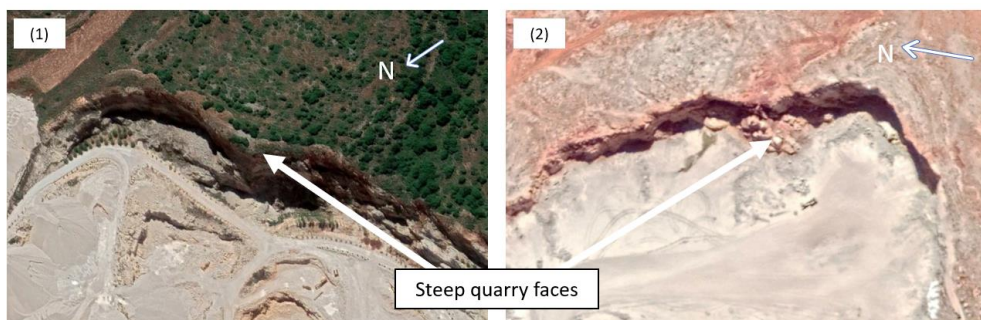


Figure 3: Images by Google Earth of the quarry faces shown in Figure 2

The aim of the current work is to further develop the assessment that Kaafarani (2020) initiated and to determine from multiple site-specific analyses the most likely mode(s) of failure of these steep rock slopes. The extent to which the impact of a rockfall may

reach the surrounding areas will also be assessed. The study will be conducted by performing site-specific analyses of four limestone quarries under rainfall and earthquake events. These slopes will be assessed against structurally controlled failure (failure that is developed along discontinuities) and non-structurally controlled failure (failure that is developed through the overall rock mass). The results will be extrapolated and used to predict landslide hazards and risks at quarry sites in Lebanon. Using the maximum runout distance and minimum angle of reach obtained, new recommendations will be proposed as guidelines to be considered when developing new regulations for construction near quarries. In addition, it will be also used to implement a mitigation plan to minimize the anticipated risks that may arise from existing quarries located at a distance less than the maximum runoff distance defined in this study.

1.2 Description of Selected Quarry Sites

Four limestone quarries (Aarsal, Ain Bourday, Janta, and Raiit) were selected for stability analysis. They are located in the Anti-Lebanon mountain range (Figure 4) covered mainly with limestone and chalk from the Jurassic period. These quarries operate illegally since they are not located in the permitted areas for quarrying activities (Figure 1). It is important to note that all four quarries are limestone with steep fractured slopes and that no failures were observed at these quarries at the time of the field visit.

The selection was made on the basis of accessibility to obtain permission to enter these quarries and fly a drone over them. Due to the sensitivity of this sector especially that it is usually controlled by politicians, it was easier to reach these four illegal quarries due to their location near the approved areas rather than reaching very far away quarries especially those in Mount Lebanon and near the capital Beirut

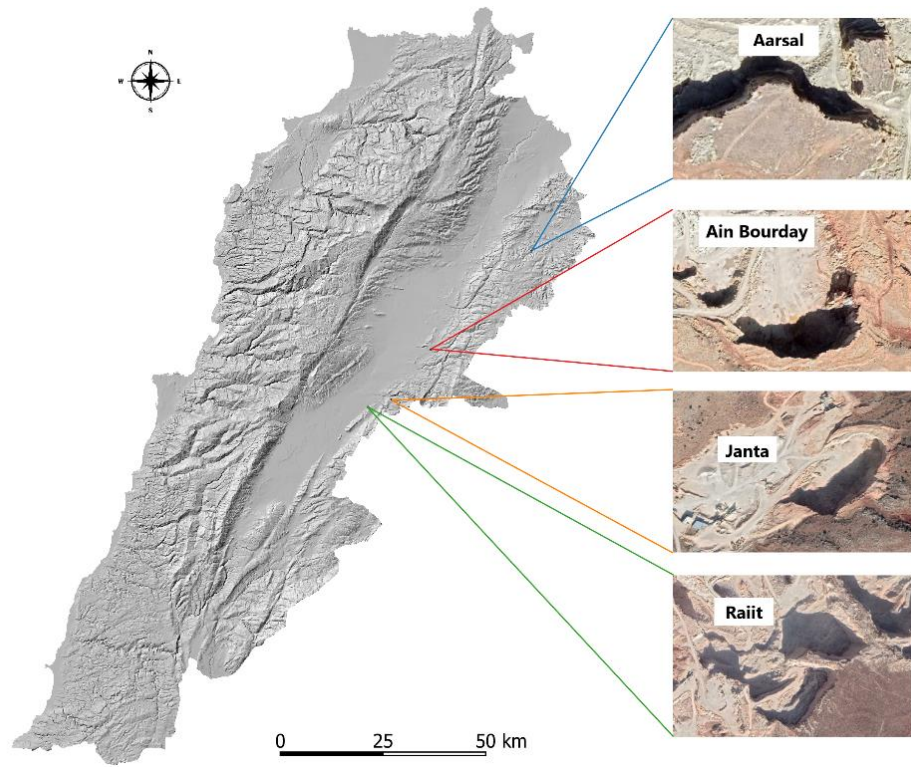


Figure 4: Locations of the study areas

Chapter Two

Literature Review

2.1 Geology, Climate, and Tectonic setting of Lebanon

Lebanon is located on the eastern shore of the Mediterranean Sea, occupying about 10,452 square kilometers. It is characterized as a mountainous country where more than one-fifth of the country is located at an altitude of 3,000 m above sea level. The country is dominated by limestone, sandstone and other sedimentary rocks, and basalt (Figure 5). About 70% of the exposed rocks are karst limestone (Nader, 2014).

The climate is characterized by long, hot, and dry summers and cool and rainy winters. Winter from December to mid-March is the rainy season, with major precipitation and mountain snow. The average rainfall ranges from 0 to 1400 mm/year (Plassard, 1971). The coastal areas of Lebanon receive between 600 and 800 mm/year of rainfall, while the mountains receive between 1000 and 1400 mm/ year. The inland Bekaa region receives between 200 and 600 mm/ year while the south of Lebanon receives between 600 and 1000 mm/year (MOE/UNDP/ECODIT, 2011).

Lebanon is a country of moderate to high seismic hazard (Harajli et al. 2002). It lies along the 1000-km-long left-lateral Levant fault system (LFS) which is responsible for a significant number of seismic events in the eastern Mediterranean (Huijer et al., 2011). The main active faults (Figure 5) are the Yammouneh, Rachaya, Serghaya and Roum faults, as well as the Mount Lebanon thrust (MLT) whose existence was recently demonstrated by SHALIMAR marine geophysical campaign (Huijer et al., 2011). Huijer (2010) and Huijer et al. (2011) conducted probabilistic seismic hazard analyses (PSHA) and found that the peak ground acceleration corresponding to 10 percent probability of exceedance in 50 years exposure time (475 years of return period

between occurrences) for most areas within Lebanon varies between 15 and 35 percent of the gravitational acceleration (Figure 22).

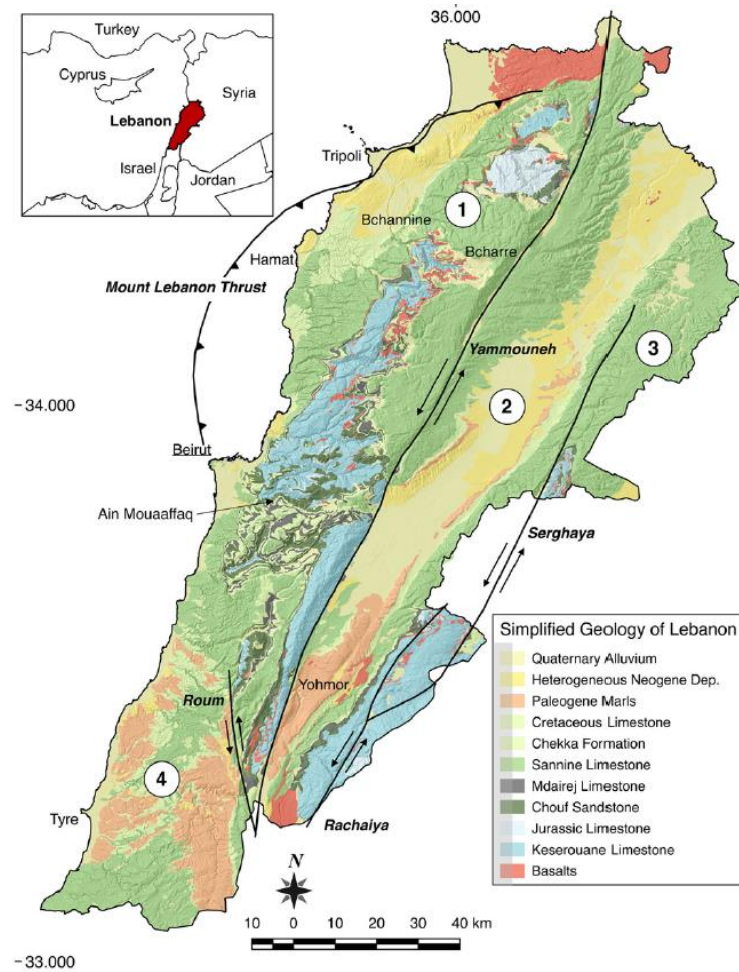


Figure 5: Major geologic units and faults (bold) of Lebanon (Source: (Grant et al. 2016))

2.2 Failures of Quarry Slopes

Many cases of quarry failures that have been recorded in the world were induced by various factors such as unpredicted environmental events and uncontrolled blasting or mining practices. This section describes different failures to highlight the importance of the human induced cases for slope failures triggered by rainfall and earthquake conditions.

2.2.1 Cases of Quarry Failures Worldwide

In September 1881, a landslide in a large quarry in Elm, eastern Switzerland killed 115 people. Quarry work began in 1861 where a semi-open tunnel, 180 meters long and 65 meters deep, was excavated into the mountain, destabilizing the slope. This steep cut caused some minor rockfall events and opened some fissures. These fissures continued to grow due to blasting work performed during the excavation until a heavy rain in 1881 caused water to seep into the cracks. This resulted in reduced shear strength along the open fractures and increased pore pressure. It ended in massive rock failure (Bressan, 2013).

Between 2005 and 2006, due to uncontrolled blasting activities and heavy rainfall, a very steep limestone quarry in Trabzon, north-eastern Turkey, experienced three separate planar failures. The failures resulted in the demolition of houses, a mosque and a school, and also adversely affected the road and farm fields surrounding the quarry (Figure 6a) (Karaman et al., 2013).

In 2015, a quarry owner died after being crushed by more than 1,000 tons of rock because of a landslide in his limestone quarry in Waikari, New Zealand (Figure 6b). The owner did not hold the Certificate of Competence that is legally required for this quarry work. The WorkSafe New Zealand investigation found that he had been operating the excavator directly under the face of the wall without monitoring or supervising the excavation activity.

On the other hand, the large landslide at the Bingham Canyon Mine in Utah, USA in 2021 is an example that shows the importance of the advanced mining industry in geotechnical monitoring and slope deformation and failure prediction. Geotechnical monitoring at that site identified the instability prior to the failure, allowing the operators to ensure that no-one was at risk. (Petley, 2021).

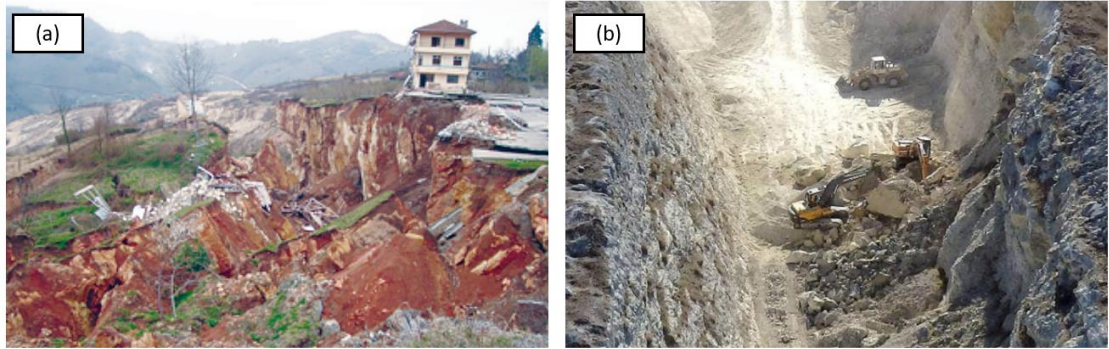


Figure 6: Quarry failure in a) Trabzon, Turkey and b) Waikari, New Zealand

2.2.2 Cases of Quarry Failures in Lebanon

In Lebanon, some examples of failures in quarries include the failure in Bjaout, Mount Lebanon (Figure 7) that occurred on February 16, 2000. The open and abandoned quarry collapsed beneath the newly constructed residential buildings. This landslide completely destroyed two buildings and the structural integrity of a third building was compromised (Abdallah, 2011; Shaban et al., 2011).

Recently, the collapse of an illegal quarry due to massive floods and mudslides in Ras Baalbek, northern Bekaa in 2018, killed a woman and destroyed her home (Moubayed, 2018). Unfortunately, no investigations have been carried out to determine the failure mechanism in the quarry.

Some other accidents at quarry sites may not be recorded because they did not cause property damage or personal injury, or because the impact was limited to quarry workers or equipment. This explains the importance of this study in evaluating the stability of illegal quarries scattered throughout the country's region to understand the mechanisms of failure of these steep slopes and thus implement a mitigation plan to reduce the risks of this hazard.



Figure 7: Residential areas threatened by quarry near Nahr El Mott, North of Beirut

2.3 Rock Mechanics Overview

In the present chapter, a brief generic overview will be given of the research into the topic of slope stability of rock slopes. The purpose of this overview is to present some of the principles of rock mechanics that have been taken into account in the analysis in this thesis.

2.3.1 Rock Mass and Intact Rock

In rock mechanics, rock mass is a matrix consisting of rock material and rock discontinuities. Discontinuity refers to the structural breaks in solid geologic materials that usually have zero to low tensile strength (Sivakugan et al., 2013). The blocks of rock material in-between the discontinuities are defined as the intact rock (Hack, 1993). The presence of discontinuities such as faults, joints and bedding planes in the rock mass affects its engineering behaviour. In fact, the rock mass is weaker than the intact rock block, showing lower strength and stiffness. Under rainfall events, the discontinuities allow greater access to water which make the rock mass more permeable and thus even weaker. This is because of the reduction of friction along

discontinuities and the increase of the pore water pressure which reduce the effective stresses and hence the shear strength. The stability of a rock slope is governed by the properties of the individual intact blocks, the frictional characteristics at the joints that separate the blocks, and the orientation of the discontinuities (Wyllie, 2015).

2.3.1.1 Properties of Intact Rock

Intact rock is a non-homogeneous, anisotropic and inelastic material and its properties of intact rock are determined by the physical properties of the materials of which it is composed and the way they are bonded to each other. The parameters which may be used in a description of intact rock include type, color, density, porosity, strength, hardness, and deformability (Zhang, 2017).

Rock type is determined from the origin of the rock that identified by the processes by which it was formed. These processes including magma cooling, sedimentation, heating or squeezing form the basis for rock classification. Rock classification is divided into three main types: sedimentary, metamorphic, or igneous rocks. Permeability of intact rock is often extremely low due to the very low porosity. The unconfined compressive strength (UCS) is most commonly used for determining the strength of intact rock and UCS stands for the maximum axial compressive stress that a cylindrical rock specimen can bear under zero confining stress (ASTM D2938-95, 2017).

Hoek and Brown (1980a, b) showed that the relationship between the major and minor principal stresses within an intact rock at failure is nonlinear (Figure 8). They proposed the following empirical equation to fit the results of a wide range of triaxial tests on intact rock samples:

$$\sigma_1 = \sigma_3 + \sigma_{ci} \left(m_i \frac{\sigma_3}{\sigma_{ci}} + 1 \right)^{0.5} \quad (2.1)$$

where σ_1 and σ_3 are the major and minor principal stresses, respectively; σ_{ci} is the unconfined compressive strength of the intact rock; and m_i is a material constant for a specific rock type.

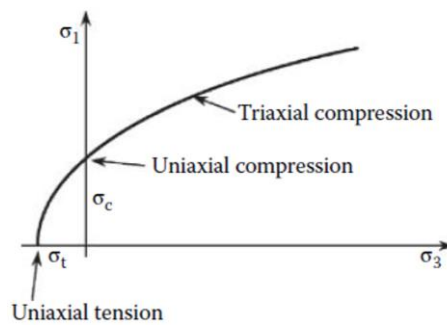


Figure 8: Hoek–Brown failure criterion

2.3.1.2 Frictional Characteristics of Discontinuities

The frictional characteristics in rock discontinuities include roughness of the surfaces, wall strength of the rock forming the walls of discontinuities, and infilling that occupies the space between the adjacent rock walls (Wyllie, 2015; Sivakugan et al., 2013). For a planar discontinuity with no infilling (Figure 9b), the shear strength will be purely frictional with zero cohesion. The friction angle will consist of two components: the residual friction angle of the rock material “ φ_b ” and the roughness angle due to interlocking of the surface irregularities or asperities “ i ” (Wyllie, 2015). Therefore, a rough surface that is initially undisturbed and interlocked will have a peak friction angle of $(\varphi_b + i)$. However, when joints are filled (Figure 9a), the shear strength must be determined based on the type of material filling the joints (Sivakugan et al., 2013).

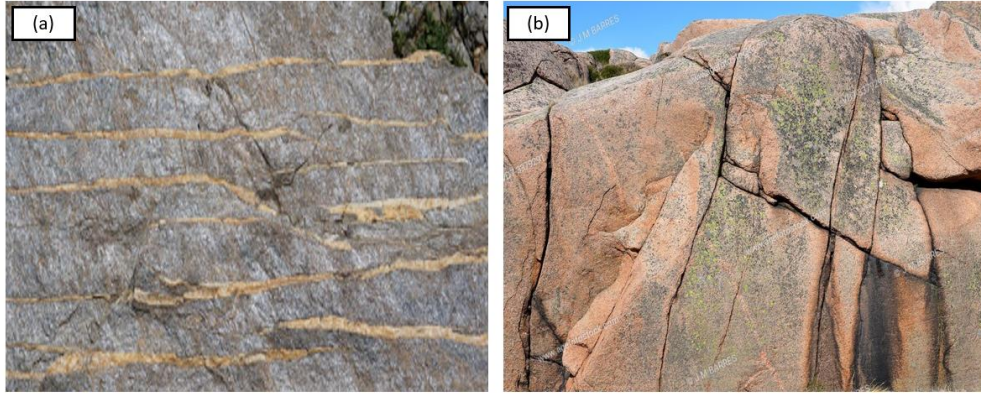


Figure 9: Joints: (a) filled and (b) unfilled

Barton and Bandis (1978) showed that the shear strength of a rough rock surface depends on the roughness, the rock strength, and the normal stress, and can be defined by the following empirical equation:

$$\tau = \sigma' \tan \left[\varphi_b + JRC \log_{10} \left(\frac{JCS}{\sigma'} \right) \right] \quad (2.2)$$

where JRC is the joint roughness coefficient, JCS is the compressive strength of the rock at the fracture surface and σ' is the effective normal stress. The joint roughness coefficient JRC is a number used to quantitatively describe the irregular morphology of joints. It can be estimated by comparing visually the appearance of a discontinuity surface with standard profiles. One of the most useful of these profile sets was published by Barton and Choubey (1977) and is reproduced in Figure 10 (Karakas, 2008). As for the joint compressive strength JRC, it can be estimated based on the compressive strength of the intact rock and the degree of weathering of rock mass that forms the joint wall.

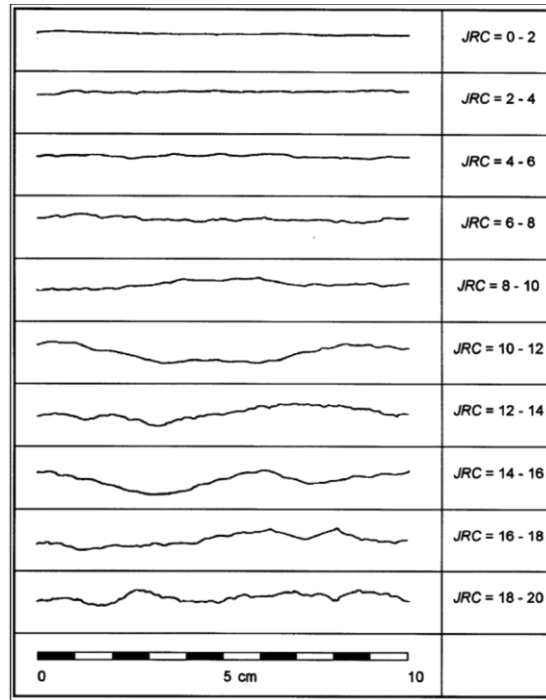


Figure 10: Roughness profiles and corresponding JRC values (After Barton and Choubey 1977)

2.3.2 Orientation of Discontinuities

The orientation of the discontinuities of rock mass has an important influence on the stability of rock slope and its possible failure mechanisms. The recommended terminology for the orientation of a plane is the dip and dip direction which are defined as follows and shown schematically in Figure 11a.

1. Dip (ψ) is the maximum inclination of a discontinuity with respect to the horizontal plane.
2. Dip direction (α) is the direction of the horizontal trace of the line of dip, measured clockwise from the north.

As for lines, the orientation is defined by plunge and trend as shown in Figure 11b.

1. Plunge (ψ) (similar to dip of a plane) is the inclination of the line with respect to the horizontal plane. It is taken as positive when the line is below the horizontal plane and negative when above.

2. Trend (α) (similar to dip direction) is the direction of the horizontal projection of the line, measured clockwise from the north.

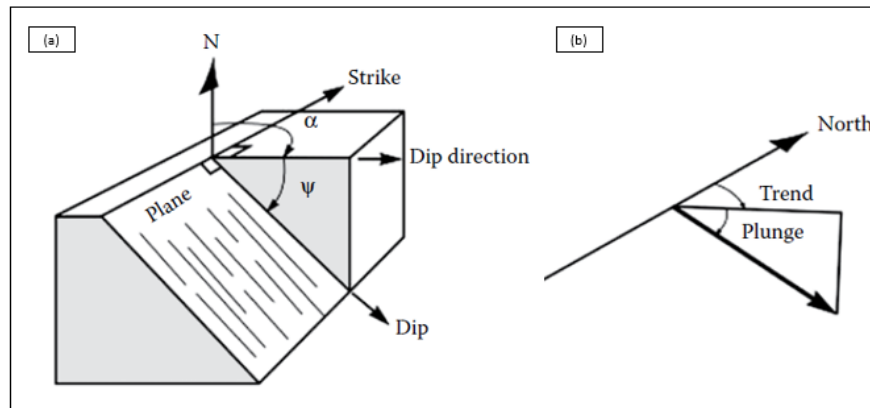


Figure 11: Terminology defining discontinuity orientation: (a) isometric view of plane (dip and dip direction); (b) isometric view of line (plunge and trend).

2.3.3 Stereographic Projections

Slope stability studies should address the structural geology of the site, and such studies involve identifying the set or sets of discontinuities that will control the analysis. The data showing the properties of these sets occur in three dimensions with a degree of natural dispersion, and in order to be able to use the data in design, the stereographic projection was found as an ideal tool for this application (Wyllie, 2015).

The stereographic projection allows the representation and analysis of three-dimensional orientation data in two dimensions where lines or points can represent planes, and points can represent lines. Figure 12a shows how a plane can be fully defined by a great circle (the intersection of the plane with the reference sphere) or a pole (the point on the surface of the reference sphere that is pierced by a radial line in a direction normal to the plane). Figure 12b shows how a line can be only defined by a pole (the intersection of the line with the reference sphere).

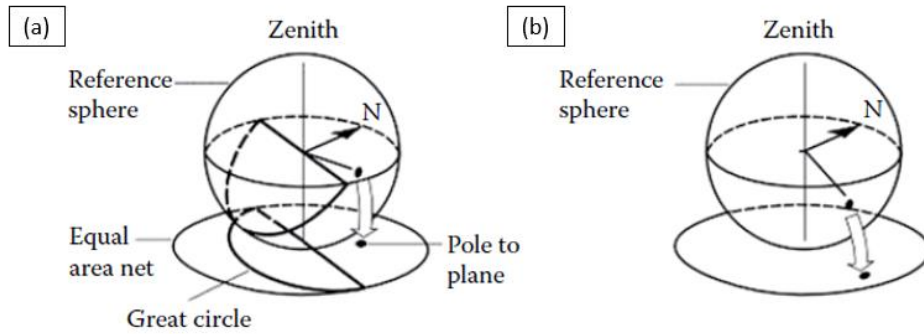


Figure 12: Equal area projections of plane and line: (a) plane projected as great circle and corresponding pole; (b) line projected as pole (Source: Wyllie, 2015)

The two types of stereographic projections used in structural geology are the polar and equatorial projections as shown in Figure 13. The equatorial stereonet is used to present the projection of a great circle and a pole while the polar stereonet is used to plot only poles.

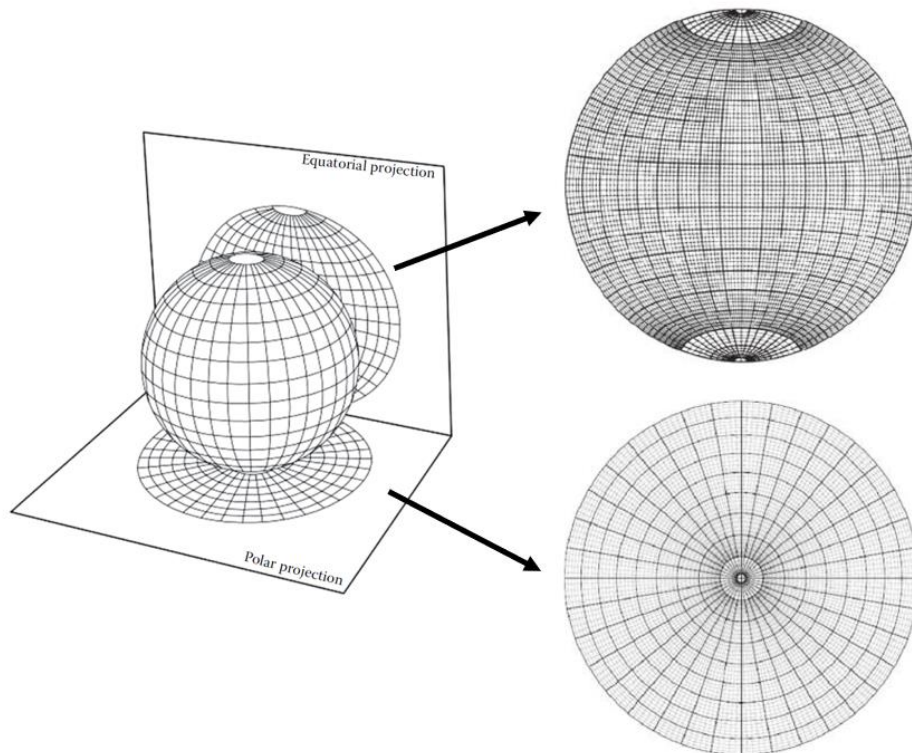


Figure 13: Polar and equatorial projections of a sphere.

To illustrate this point, the orientation of two joint sets J1 and J2 is defined by their dip and dip direction as 20/150 and 85/340, respectively. Figure 14a shows a pole plot of

the poles for the two planes as well as their great circles and Figure 14b shows their corresponding isometric view. This example shows that the steeper the plane, the further is the pole from the center; the J2 pole is furthest from the center and the J1 pole is closest to it. Moreover, it shows a limitation of stereographic projections that only consider angular relationships between lines and planes, and do not represent their physical position or size (Wyllie, 2015).

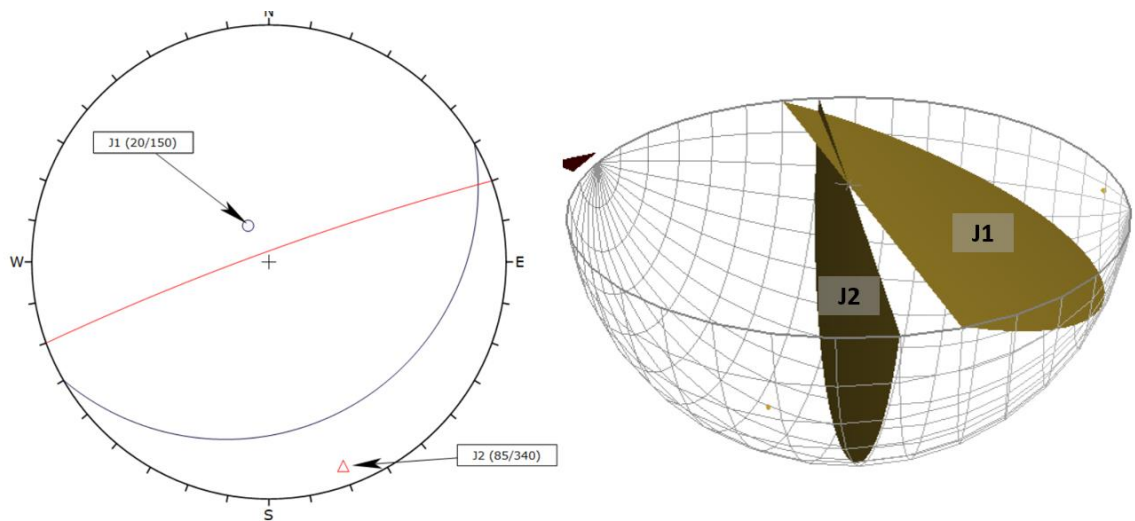


Figure 14: (a) A pole plot and (b) an isometric view of the three planes.

2.4 Discontinuities Mapping Techniques

In the stability analysis of rock slopes, the first step is to perform a rock mass characterization that determines the quality of rock masses (Bar et al., 2021). The properties of interest in rock mass are mainly the existing discontinuity sets, their orientations, location, spacing, persistence and roughness. This can be performed using two different methods: traditional mapping technique by field survey or digital mapping techniques using data from remote sensing.

2.4.1 Traditional Mapping Technique

Geotechnical engineers traditionally characterize rock masses by geological and geotechnical surveys, which combine visual and manual technologies to characterize

rock masses. The traditional scanline mapping technique is usually adopted which involves drawing a line over an outcropped rock surface using a tape and measuring and describing all discontinuities that intersect this line (Chaminé et al., 2014). However, this method is time consuming and limited to sites that are easy for surveyors to access and which do not threaten their safety during operation (Riquelme et al., 2017).

2.4.2 Remote Sensing Techniques

As an alternative, the recent development of new remote sensing techniques allows the acquisition of all 3D information about a rock slope without making any physical contact with it. They are used to produce a 3D point cloud data and a 3D terrain model of the surveyed area from which strength properties of the rock mass can be inferred. The Point cloud data can be produced directly with laser scanning (LiDAR), terrestrial (TLS) or aerial (ALS) or produced by means of applying Structure from Motion Multi-View Stereo (SfM-MVS) algorithms, using platforms as Unmanned Aerial Vehicle (UAV) (Robiati et al., 2019). Laser scanning requires the use of a lidar instrument (Figure 15b) which sends pulsed laser light and measures the reflected pulses with a sensor which are used to obtain the coordinates (X, Y, and Z) of the points that form the slope surface (Riquelme et al., 2017). A limitation of this ground-based remote sensing method using lasers is related to the survey of high slopes and complex shapes where the site of acquisition, generally at the bottom of the slopes, leads to occlusion zones and shadows in the output data (Bar et al., 2021). Such limitation can however be overcome by using the Structure from Motion (SfM) methods, with which high-detail images can be obtained using UAV (Figure 15b) even in the case of high-steep slopes. The captured images are converted into accurate point cloud data using photogrammetry software for drone mapping such as the PIX4Dmapper and

ShapeMetriX 3D programs. The accuracy of this method is highly dependent on the resolution of the camera (Riquelme et al., 2017). This technique (SfM) is now widely used in rock slope stability analysis (Bar et al., 2021; Suri et al., 2020; Wang et al., 2019; Manousakis et al. 2019) because of the advanced fundamental principles of photogrammetry and the available powerful algorithms that make the acquisition of a unique three-dimensional location of a set of given points from the captured raw images faster and less expensive than the TLS.

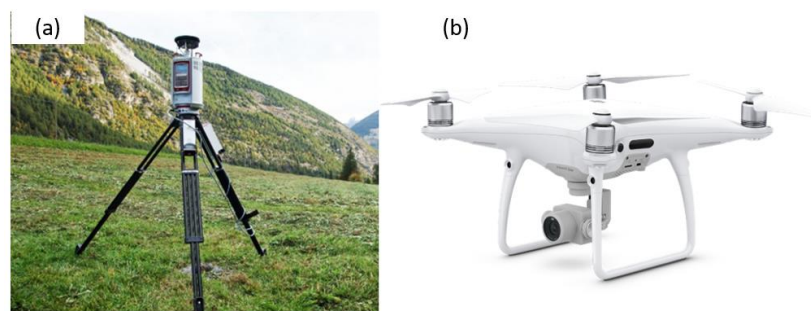


Figure 15: The two instruments used in remote sensing technology: a) TLS and b) SfM

Once the 3D point cloud is generated, the properties of the discontinuities are detected manually or semi-automatically using available, open-source algorithms. For instance, some authors (Suri et al., 2020; Riquelme et al., 2017) used the MATLAB's open-source Discontinuity Set Extractor (DSE) software while others (Manousakis et al. 2019) recently used ShapeMetrix UAV (3GSM GmbH, Austria) software. DSE was programmed by Adrián Riquelme for testing part of his PhD studies aimed at extracting discontinuity sets from a rock mass. Riquelme et al. (2014) tested the algorithm on a cube shape and on an actual slope with visible discontinuities by performing a complete sensitivity analysis of the statistical parameters that should be used in order to perfectly detect the orientation of the planes. The proposed optimal values were then verified by presenting a case study analyzing the stability of a rock slope in the district of San Blas, Spain. The input data for DSE is a 3D point cloud

which is analyzed and exported into different point cloud files where each joint set is represented by different colours. All detected joint sets in DSE should be overlaid on the quarry face in CloudCompare software to be validated, and only points tracing actual discontinuities should be kept while points tracing parts of the slope surface and curvature should be discarded. The main advantage of using DSE and CloudCompare is that both programs are freely available to users unlike ShapeMetriX 3D software package where the user has to get a paid license. However, ShapeMetriX allows the user to perform image processing and discontinuity detection as well as geometric measurements including volumetric measurements in the same software.

2.5 Rock Slope Failure Mechanisms

The modes of rock slope failure depend mainly on the geometric interaction of existing discontinuities and the strength of the rock material between them (intact rock strength) (Hudson & Harrison, 1997; Sivakugan et al., 2013). These modes can be basically grouped into two categories, i.e., “structurally controlled failure” and “non-structurally controlled failure”. Structurally controlled failure often occurs along specific pre-existing discontinuities (Figure 16a) typically in hard rock with large discontinuity spacing (Hudson & Harrison, 1997; Goodman, 1989). Non-structurally controlled failure occurs along a surface that approaches a circular shape (Figure 16b) in weak, highly weathered and/or closely fractured rock (Wyllie, 2015). Although most rock slope instabilities are controlled by the geological structures (Hudson & Harrison, 1997), it is always necessary to assess overall slope stability, especially if the strength of the intact rock is low and/or the spacing between discontinuities is small which makes the rock mass highly fracturing.

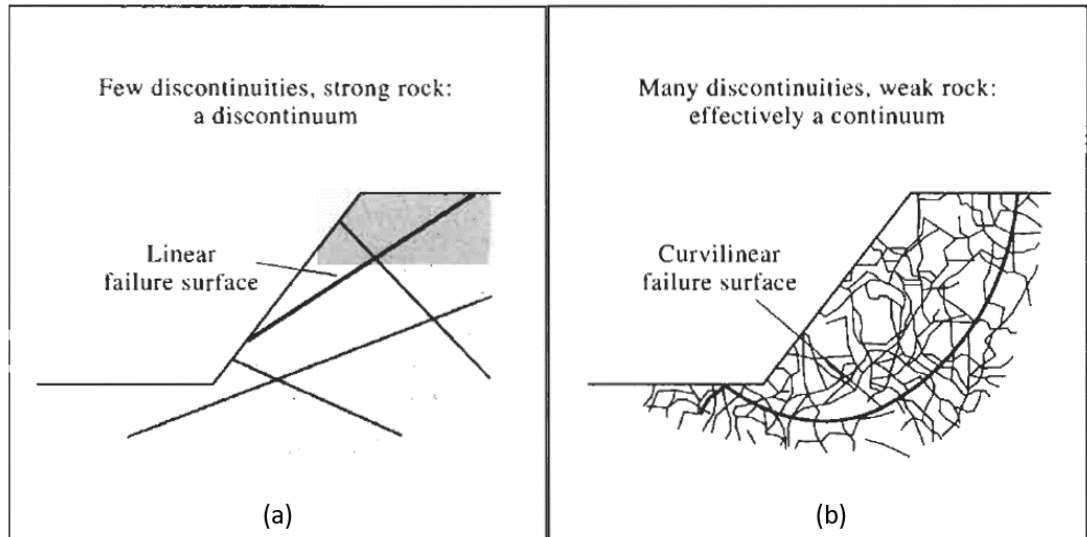


Figure 16: Slope failure mechanisms: a) structurally controlled failure b) non-structurally controlled failure.
Source: (Hudson & Harrison, 1997)

2.5.1 Structurally Controlled Failure

In a structurally controlled failure, rock slope stability is governed primarily by the presence of pre-existing geological discontinuities within the rock mass. The first step to assess structurally controlled failure is to perform a kinematic analysis that predicts the potential structural failure mechanisms (planar, wedge, or toppling) by studying the relationship between the orientations of the discontinuity and the orientation of the slope face (Wyllie, 2015). This method is usually done by first performing a stereonet projection of the joint sets in addition to the orientation of the slope face (Basahel & Mitri, 2017). Once the kinematic analysis is performed, limit equilibrium (LEM) and/or finite element methods (FEM) are used to obtain the slope stability factor of safety.

2.5.1.1 Kinematic Analysis

The following sections present the conditions under which a particular failure mode occurs and the way to check them easily using stereonet projections.

Planar Sliding:

Planar sliding occurs on a discontinuity plane dipping out of the slope face at an angle smaller than the slope angle and greater than the friction angle of the discontinuity surface and striking parallel or nearly parallel to the slope face. These conditions can be checked by using spherical projections. For plane failure to occur along a certain discontinuity, its pole must fall within the critical zone for planar sliding as shown in Figure 17. This zone is enclosed between the friction cone, representing the residual friction angle along the discontinuity, the slope plane representing the orientation of the slope face, and the lateral limits to ensure that the dip direction of the discontinuity is within a certain angular range of the slope face dip direction.

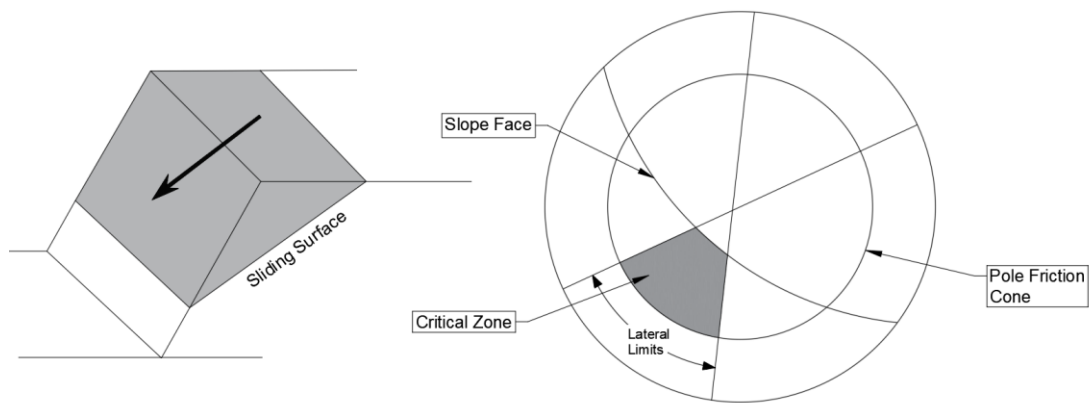


Figure 17: Planar sliding kinematic analysis

Wedge Sliding

Wedge sliding occurs when the line of intersection of two discontinuities is daylighting into the slope face at an inclination significantly greater than the average angle of internal friction of the two joint/bedding materials. These conditions can be also checked by using spherical projections. For wedge failure to occur along two discontinuities, the pole of the line representing the intersection of these two planes must lie within the critical zone for wedge sliding as shown in Figure 18. This zone is enclosed between the friction cone and the slope plane.

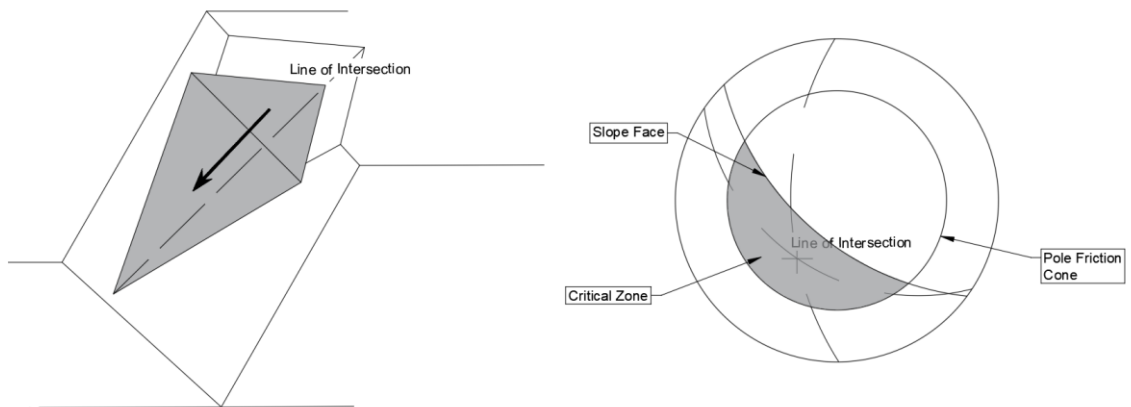


Figure 18: Wedge sliding kinematic analysis

Toppling Failure

Toppling failure occurs when multiple rock columns or layers (depending on their dimensions) are steeply dipping into the slope face causing them to rotate about their bases into the free excavation (Fig. 20c) (Hudson & Harrison, 1997; Sivakugan et al., 2013). For toppling failure to occur over a certain discontinuity, its pole must lie within the critical zone for toppling failure as shown in Figure 19. This zone is defined by the region outside the slip limit plane and inside the lateral limits. The slip limit plane is not an actual physical plane although it is derived from the slope angle and friction angle. The dip angle of the slip limit plane is equal to the difference between the slope dip and the friction angle, and its dip direction is equal to that of the slope face.

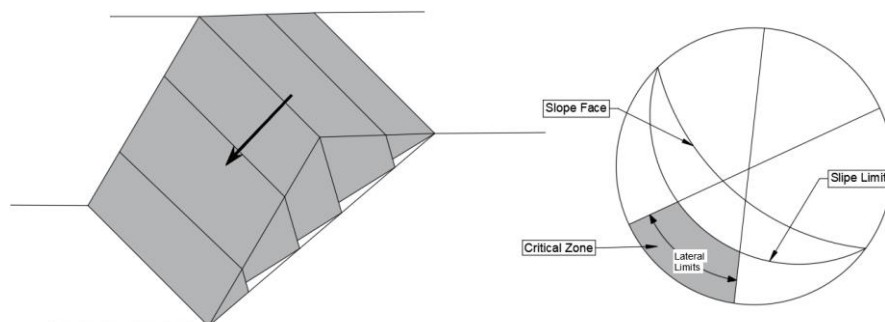


Figure 19: Kinematic analysis toppling failure

If a failure mode is determined to be kinematically admissible, in another term if the conditions stated above are satisfied, the slope stability for that particular failure mode should be analyzed using LEM or/and FEM in order to determine the slope safety factor under consideration.

2.5.1.2 Limit Equilibrium Method

Limit equilibrium methods are widely used to examine the structural stability of slopes by comparing the magnitudes of the driving and resisting forces that act along the sliding planes to estimate the factor of safety (Sivakugan et al., 2013). The latter is then defined as the ratio of the summed resisting forces to driving forces computed purely on the principles of statics. The resisting forces are determined based on the shear strength of rock discontinuities directly related to their surface roughness which is estimated based on Barton-Bandis criterion discussed in section 2.3.1.2 Frictional Characteristics of Discontinuities. This method provides reasonably reliable results with limited required input; however, it does not take into account the stress-strain relationship in the analysis, thus it cannot compute displacement and cannot model progressive failure (Memon, 2018).

2.5.1.3 Finite Element Method

Another method of assessing the structurally controlled failure is by adopting the finite element method (FE). FE methods have gained more attention due to their ability to overcome the limitations of LE methods. One method of finite element slope stability analysis is the Shear Strength Reduction (SSR) technique in which the shear strength parameters (friction angle and cohesion) are gradually reduced until failure occurs. The reduction factor that causes the failure is reported as the factor of safety of the slope under study (Matsui and San, 1992). However, according to a study by Cheng et al. (2006) aimed to compare the two methods, it was concluded that each method has

its advantages and limitations, and that the use of FE methods is not superior to the use of the LE methods in routine analysis and design. These methods have been used in several studies to assess the stability of rock slopes in general, and quarried slopes in particular.

2.5.2 Non-Structurally Controlled Failure

Although most of the stability of rock slopes is controlled by their geological features, it is necessary to assess the general slope stability in case of a closely fractured, highly weathered, or weak rocks. In these conditions, failure surface is free to find the line of the least resistance through the slope. This analysis is performed using the slope height, slope angle, and shear strength of the rock mass. In order to estimate the latter, geotechnical engineers classify the rock mass and relate the strength to the classification associated with it. Some of the common rock mass classification systems are Rock mass rating (RMR), Q-system, and Geological strength index (GSI). The Hoek Brown failure criterion and the associated GSI have gained wide acceptance as tools for estimating the strength and deformation characteristics of heavily jointed rock masses especially since the first two classification system mentioned were primarily developed for tunnelling work. We discussed in Section 2.3.1.1 Properties of Intact Rock the Hoek-Brown criterion to quantify the strength of intact rocks. This criterion has evolved over the years into a more generalized Hoek–Brown criterion for estimating the strength of rock masses as well as intact rocks. It is expressed as:

$$\sigma_1 = \sigma_3 + \sigma_{ci} \left(m_b \frac{\sigma_3}{\sigma_{ci}} + s \right)^a \quad (2.3)$$

where m_b , s , and a are the rock mass material constants, given by:

$$m_b = m_i \exp \left[\frac{GSI-100}{28-14D} \right]$$

$$s = \exp \left[\frac{GSI-100}{9-3D} \right]$$

$$a = \frac{1}{2} + \frac{1}{6} (e^{-GSI/15} - e^{-20/3})$$

The GSI value is assigned using Figure 20 and the disturbance factor D is estimated based on the degree of disturbance to which the rock mass has been subjected to blast damage and stress relaxation. The value of D varies in the range of 0–1; 0 for undisturbed and 1 for highly disturbed rock mass.

| GEOLOGICAL STRENGTH INDEX FOR JOINTED ROCKS (Hoek and Marinos, 2000) From the lithology, structure and surface conditions of the discontinuities, estimate the average value of GSI. Do not try to be too precise. Quoting a range from 33 to 37 is more realistic than stating that GSI = 35. Note that the table does not apply to structurally controlled failures. Where weak planar structural planes are present in an unfavorable orientation with respect to the excavation face, these will dominate the rock mass behavior. The shear strength of surfaces in rocks that are prone to deterioration as a result of changes in moisture content will be reduced if water is present. When working with rocks in the fair to very poor categories, a shift to the right may be made for wet conditions. Water pressure is dealt with by effective stress analysis. | | SURFACE CONDITIONS | | | | |
|---|---|---|--|---|--|--|
| | | VERY GOOD Very rough, fresh unweathered surfaces | GOOD Rough, slightly weathered, iron stained surfaces | FAIR Smooth, moderately weathered and altered surfaces | POOR Slackensided, highly weathered surfaces with compact coatings or fillings or angular fragments | VERY POOR Slackensided, highly weathered surfaces with soft clay coatings or fillings |
| STRUCTURE | | DECREASING SURFACE QUALITY | | | | |
|  | INTACT OR MASSIVE – intact rock specimens or massive <i>in situ</i> rock with few widely spaced discontinuities | 90 | | | N/A | N/A |
|  | BLOCKY – well interlocked undisturbed rock mass consisting of cubical blocks formed by three intersecting discontinuity sets | 80 | 70 | | | |
|  | VERY BLOCKY – interlocked, partially disturbed mass with multi-faceted angular blocks formed by 4 or more joint sets | | 60 | 50 | | |
|  | BLOCKY/DISTURBED/SEAMY – olded with angular blocks formed by many intersecting discontinuity sets. Persistence of bedding planes or schistosity | | | 40 | | |
|  | DISINTEGRATED – poorly interlocked, heavily broken rock mass with mixture of angular and rounded rock pieces | | | | 30 | 20 |
|  | LAMINATED/SHEARED – lack of blockiness due to close spacing of weak schistosity or shear planes | | | | | 10 |
| | | | | | | |

Figure 20: Geological Strength Index Chart for Jointed Rocks.

2.6 Example of Slope Stability Analysis based on Structurally Controlled Failure

Salvini et al. (2013) evaluated the stability of a mountain slope in Italy using data derived from Digital Terrestrial photogrammetry. The geometrical and structural characteristics of the slope, such as joint attitude, spacing and persistence, and block volumes, were obtained from the built 3D digital model. Kinematic analysis was then carried, and the slope was found to be prone to wedge failure and planar failure. Hence, the programs Rocplane and Swedge (RocScience) were used to simulate the sliding of blocks along planes and lines of intersection between joints on the basis of limit equilibrium methods. The Barton-Bandis criterion was applied to estimate the shear strength along discontinuities. The probabilistic distribution of the rockfall end points and kinetic energy along the rock falling paths were evaluated to create a hazard map based on the spatial distribution of trajectories, rock fall transit density and kinetic energy.

Abdullah et al. (2018) assessed the stability analysis of a sandstone quarry located in Karang Sambung district, Indonesia. The quarry face is 6 to 7 meters high and has a steep angle of 80° to 90°. In this study, the properties of the major three discontinuity including orientations, spacing, and filling materials were determined using traditional vertical and horizontal scanline mapping. In DIPS software by RocScience, kinematic analysis showed that the slope has a high probability of wedge failure. The slopes were then analysed using limit equilibrium methods in RocScience SWEDGE software and finite element methods in RocScience RS2 software. The results showed that the slope is unstable based on the LE methods with factor of safety less than 1 but stable based on FE methods with factor of safety greater than 1 which make the latter less conservative.

Similarly, Robiati et al. (2019) evaluated the rockfall potential within a quarry slope at Treviscoe Pit in UK based on back analysis of a rockfall event that initially occurred in 2011 and developed into a full slope scale activity in 2013, including a major event in early 2016 with further ongoing activity. Through analysis of 3D point cloud data obtained from aerial and terrestrial LiDAR from 2011 up to the date of the study, an investigation was undertaken to characterise the orientation of discontinuities present within the rock slope using SplitFX software. Kinematic analysis was then performed in RocScience DIPS software, highlighting the potential for both direct and oblique toppling failures. These findings validate the capability of the Unmanned Aerial Vehicle (UAV)-based 3D photogrammetric analysis to inform back analyses of the underlying failure mechanism and investigate potential runout.

Saroglou et al. (2019) presented the UAV-based mapping and subsequent slope stability analysis of recent failure along the Corinth Canal. Since the beginning of the operation of this channel, in 1893, the slopes have experienced stability problems due to the very steep inclination, the mechanical behavior of the Corinth Canal marl and the strong earthquakes that have affected the region. In this study, the authors first determined the geometry of the faults and main discontinuity sets from the 3D photogrammetric models using photos captured from the UAV and the ShapeMetriX UAV (3GSM GmbH, Austria) software. Then, an initial stability assessment of the slope was conducted using a 2D limit equilibrium analysis against planar sliding using Rocplane by RocScience. Followed by a 3D limit equilibrium analysis, Slide3 by RocScience was used to model the 3D nature of the slope failure more accurately. 2D and 3D analysis showed failure surfaces very similar to the actual failure event. Moreover, the adopted methodology has also proven to be effective in back calculating the strength of the failed rock mass.

Bar et al. (2021) presented two case studies from San Leo cliff in Italy and an open pit mine in the Caribbean in which remote reconnaissance using UAV is used to classify natural and engineering rock slopes. Q- Slope method was adopted to assess the stability of excavated rock slopes. This method has been developed by supplementing Q-system with orientation weightings (O-factors). The results showed that the benefit of combining UAV photogrammetry and Q-slope is the ability to rapidly create an accurate topographical survey and to derive geological structure information in areas that are not safely accessible by people.

Chapter Three

Methodology

This chapter outlines the methodology that was adopted to assess the stability of four limestone quarries located in the Anti-Lebanon mountain range under dry, rainfall, and seismic conditions. The flowchart in Figure 21 sets out the methodology of this research. The first step was to visit the quarry sites where photogrammetric surveys were carried out using UAV technology to create 3D models of the rock faces for rock mass characterization, slope stability analysis, and feature extraction. The stability of the studied quarries controlled by geometry and strength of the discontinuities was evaluated kinematically and then analyzed using limit equilibrium methods under dry, rainfall, and seismic conditions. The overall stability of the quarries was also assessed based on the geological strength index (GIS) classification and the rock mass geomechanical properties were based on the generalized Hoek- Brown constants. The maximum runout distance and the corresponding angle of reach were determined wherever the quarry face was found unstable.

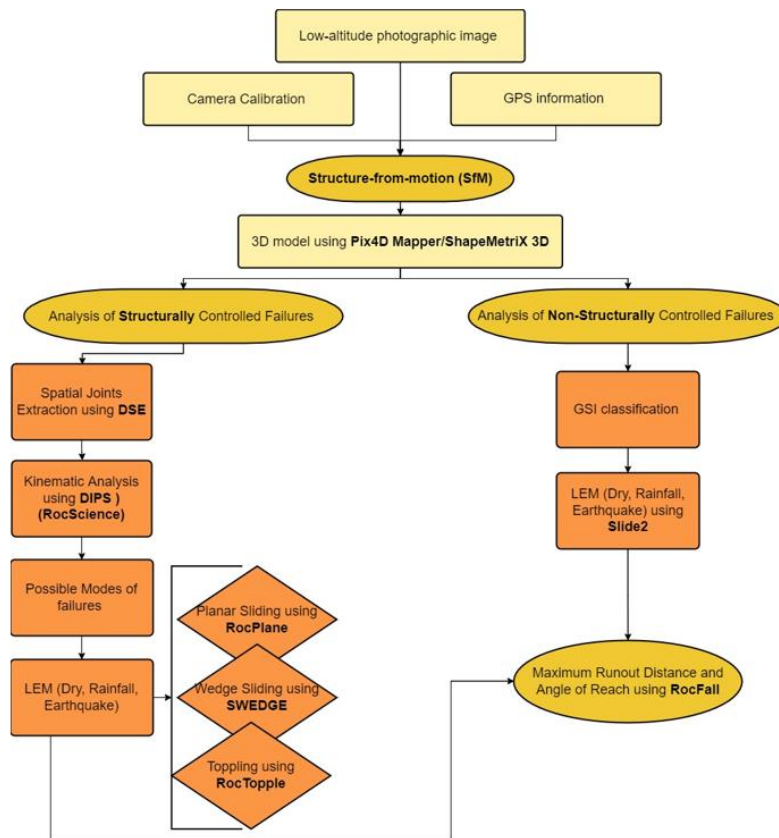


Figure 21: Methodology Flowchart

3.1 Different Software Used in this Research

This section outlines the software used in this work. More details regarding the needed parameters and data for each software are elaborated in the sections below.

- Pix4D Mapper: This software was used to construct the 3D models of the quarry faces using the captured images. It generates a 3D point cloud file which was used to detect the rock mass properties.
- CloudCompare: this software was used to visualize the 3D models, to crop selected parts and to verify the semi-automatic detection of discontinuities and slope face orientations.
- ShapeMetriX: this software was used to measure the dip and dip direction of planes defined manually.

- DIPS by RocScience: this software was used to perform the kinetic analyses using stereonet projection. The program identifies the discontinuities that show a risk of planar, wedge and toppling failures,
- RocData by RocScience: this software was used to identify the strength parameters along the discontinuities and of the rock mass from a database of predefined properties of limestone slopes.
- RocPlane by RocScience: this software was used to perform a limit equilibrium analysis to identify the factor of safety along the discontinuity showing a risk of planar sliding.
- Swedge by RocScience: this software was used to perform a limit equilibrium analysis to identify the factor of safety along the discontinuities showing a risk of wedge sliding.
- RocTopples by RocScience: this software was used to perform a limit equilibrium analysis to identify the factor of safety along the discontinuities showing a risk of toppling failure.
- Slide2 by RocScience: this software was used to perform a 2D limit equilibrium analysis of rock face based on rock mass strength parameters.
- RocFall by RocScience: this software was used to identify the maximum runout distance and the corresponding angle of reach wherever the quarry face was found unstable.

3.2 Definition of Parameters Used

The probabilistic seismic hazard assessment (PSHA) map by Huijter et al. (2011) (Figure 22) was used to select the peak ground acceleration (PGA) adopted for seismic stability analysis with 10% exceedance probability in 50 years. Likewise, a saturation map (Figure 23) generated using the Average Annual Rainfall map (Plassard, 1971)

was used for stability analysis of rainfall induced landslides. This map was scaled based on the max daily rainfall depth for 10-year return period (Pollock et al., 2019). The data used in this work is summarized in Table 1.

Table 1: Sites Description

| Location | Rock Type | Height | PGA | Precipitation | Saturation |
|-------------|-----------|--------|-------|---------------|------------|
| | | (m) | (g) | (mm/d) | (%) |
| Aarsal | Limestone | 40 | 0.225 | 97.2 | 16 |
| Ain Bourday | Limestone | 40 | 0.25 | 97.2 | 16 |
| Janta | Limestone | 40 | 0.25 | 100.1 | 17 |
| Raiit | Limestone | 50 | 0.25 | 100.1 | 17 |

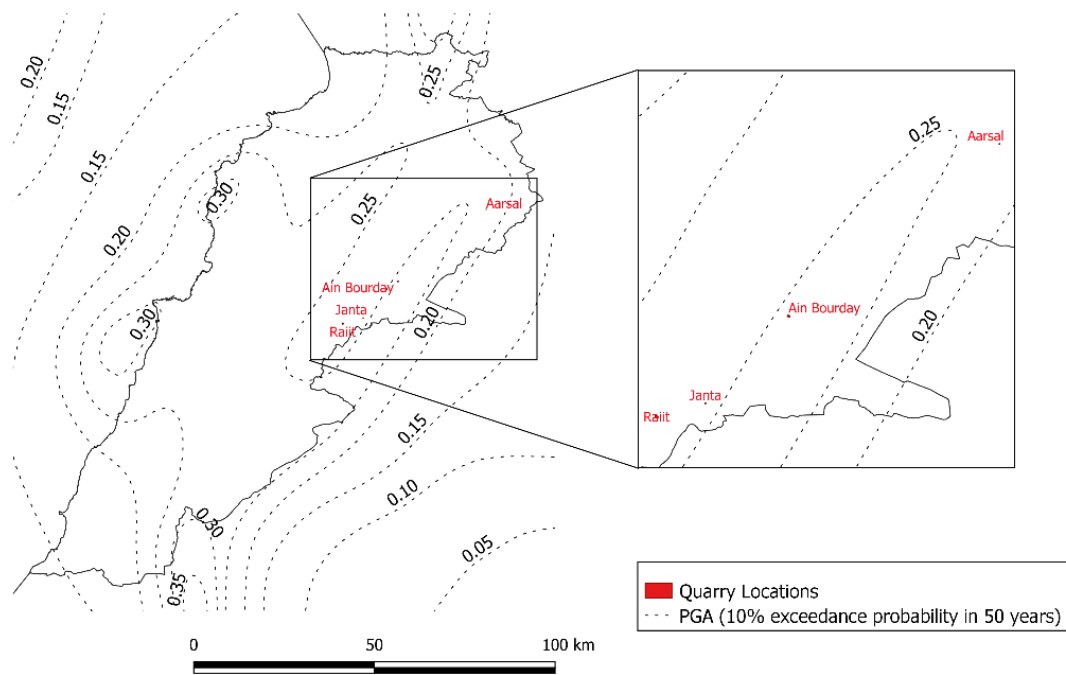


Figure 22: Contour maps of peak ground acceleration (PGA) with a 10% exceedance probability in 50 years (Huijer et al., 2011)

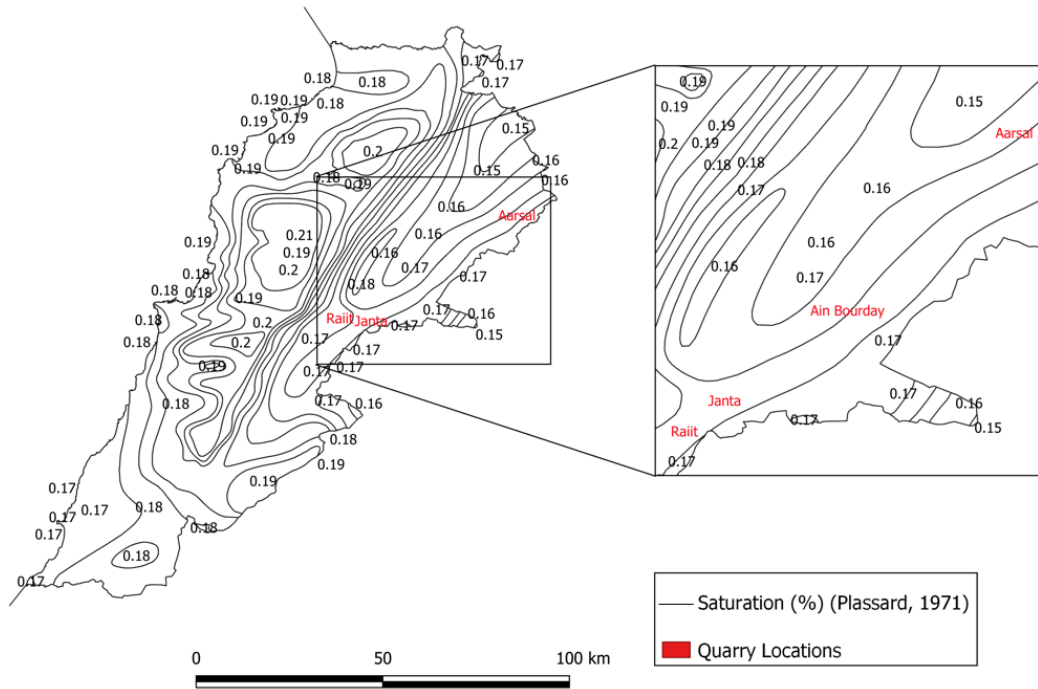


Figure 23: Level of Saturation (%) (Plassard, 1971)

3.3 UAV-based Remote Sensing Survey

The DJI Phantom 4 Pro was used to capture the digital images (Figure 24). This drone has a high-quality camera allows it to take sharp, 1080-pixel photos. It can take off and land in small areas due to its small size. One battery allows a maximum flight time of 30 minutes. When more time was required to complete the mission in progress or to start a new mission on the same visit, the battery was sequentially replaced on site with two fully charged batteries.



Figure 24: UAV operation in Quarry 2 mapping.

The UAV-based remote sensing survey consists of creating a 3D point cloud data that is defined by overlapping at least two images taken from different positions. A point cloud is a digital 3D representation of a physical object or space. It's made of a huge collection of tiny individual georeferenced points plotted in 3D space. When there is a high overlap between the images, the common area captured will be larger and thus the 3D points can be computed more accurately. The drone flight was planned using the Pix4Dcapture mobile app with a double grid mission and maximum overlap. The overlap of the side and front images was set to 90% and the camera angle was set to 60° from the horizontal based on the recommendations developed by Pix4D company for steep slope mapping (Figure 25).

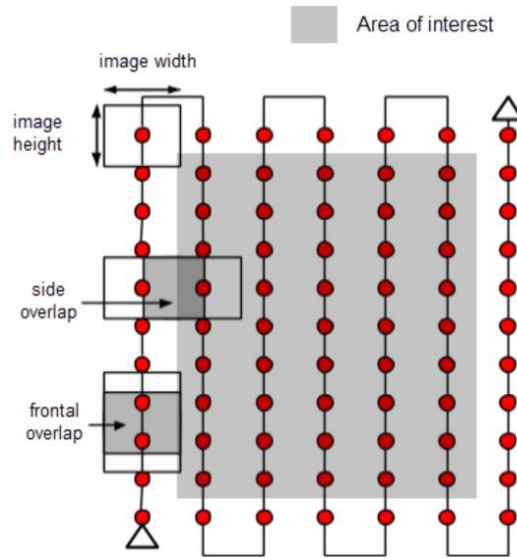


Figure 25: Image Acquisition Plan

The Pix4Dmapper software was then used to process and convert the raw photos into a 3D model including point cloud dataset, digital surface model (DSM), orthomosaic and 3D texturized mesh.

By comparing the on-site images of the four quarries to their corresponding three-dimensional models as shown in figures below (Figure 26 to Figure 29), it is evident that the generated 3D scenes match exactly the actual quarry faces.

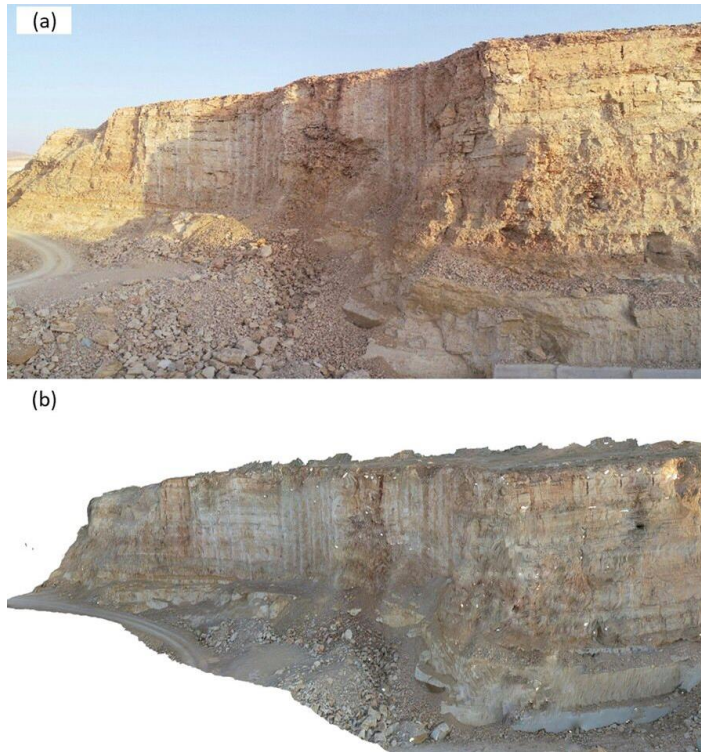


Figure 26: Aarsal Quarry: a) Image by the DJI Phantom 4 Pro drone and b) 3D Model created using the SfM technique

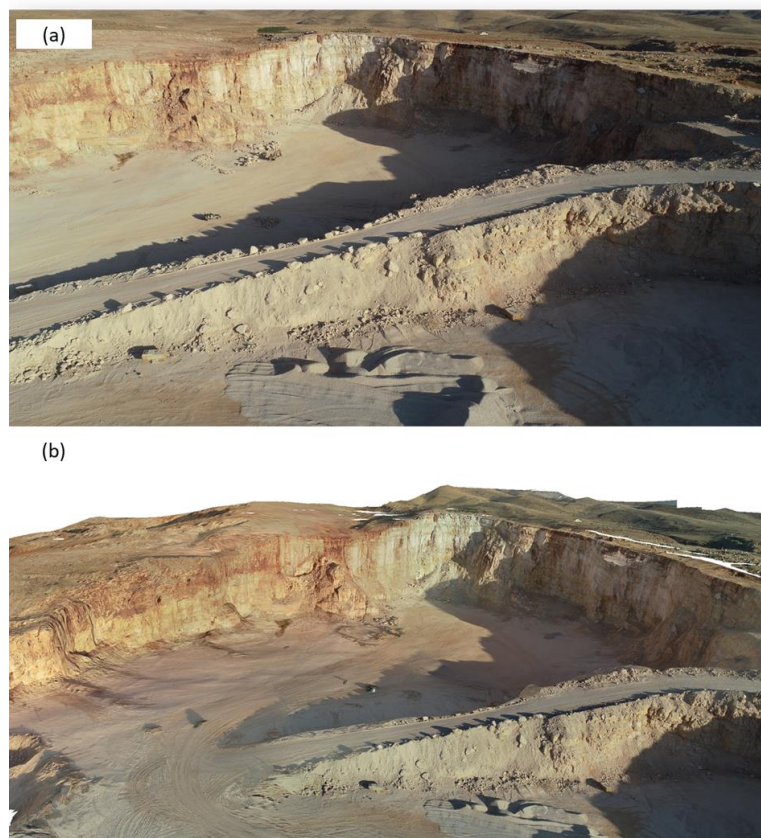


Figure 27: Ain Bourday Quarry: a) Image by the DJI Phantom 4 Pro drone and b) 3D Model created using the SfM technique

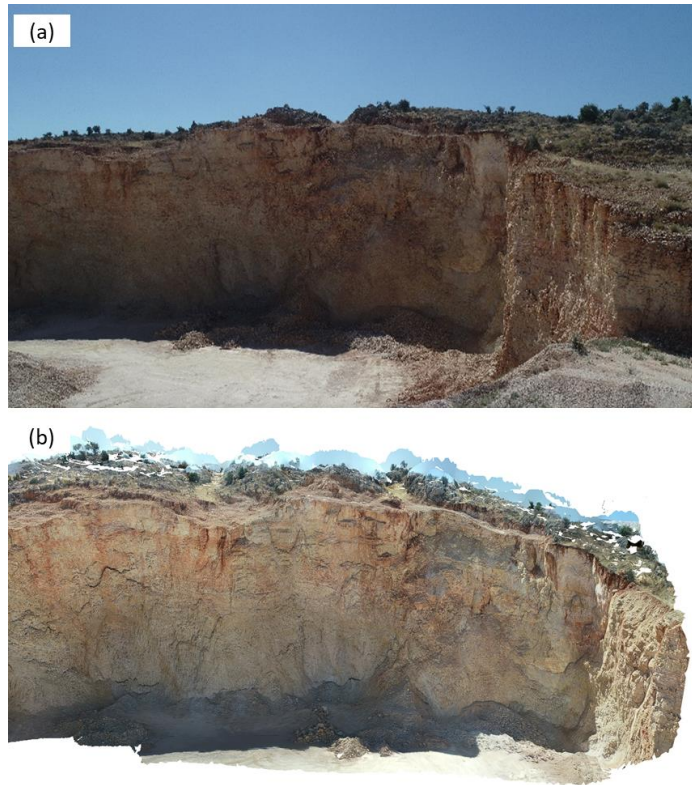


Figure 28: Raiti Quarry: a) Image by the DJI Phantom 4 Pro drone and b) 3D Model created using the SfM technique

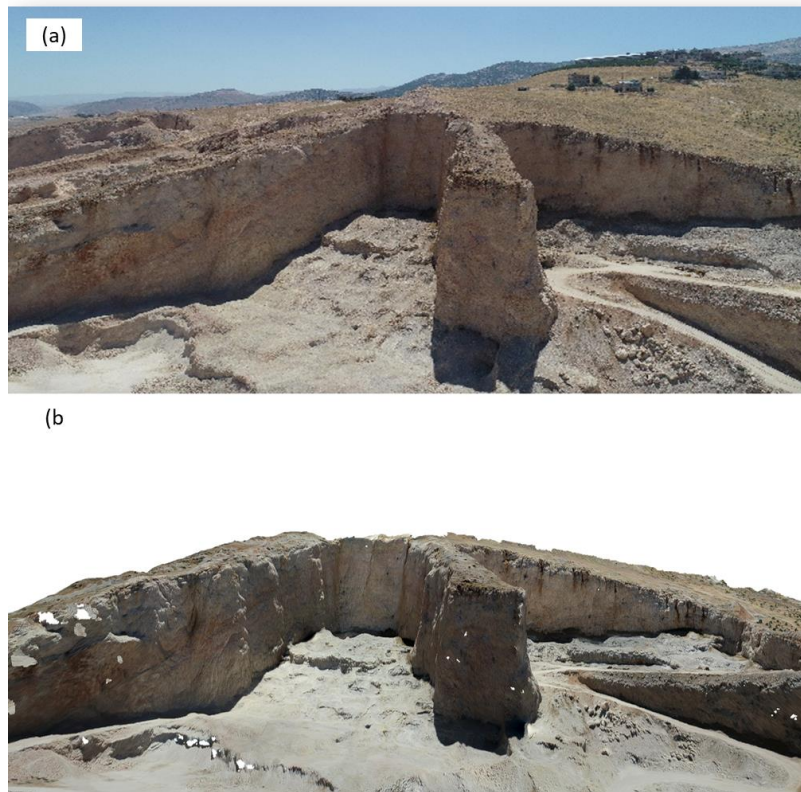


Figure 29: Janta Quarry: a) Image by the DJI Phantom 4 Pro drone and b) 3D Model created using the SfM technique.

3.4 Semi-Automated Discontinuity Extraction

To visualize and manage the 3D point clouds, CloudCompare and ShapeMetriX UAV software were used. These programs allow the user to perform projections, calculate distances, estimate geometric features such as orientation, roughness, and curvature. The generated point clouds were imported into CloudCompare software, and by visual inspection, the highly jointed slope face was selected, cropped, and saved as a separate point cloud file.

This file was then used as an input data for an open-source software programmed in MATLAB, Discontinuity Set Extractor (DSE) to extract discontinuity sets from the rock masses. DSE follows the method outlined by Riquelme et al. (2014) which defines the equations of the different planes of the rock slope surface by first applying a coplanarity test for the neighbouring points, followed by finding principal orientations and identifying clusters. Figure 30 shows an illustration of the above steps for Quarry 3 as an example.

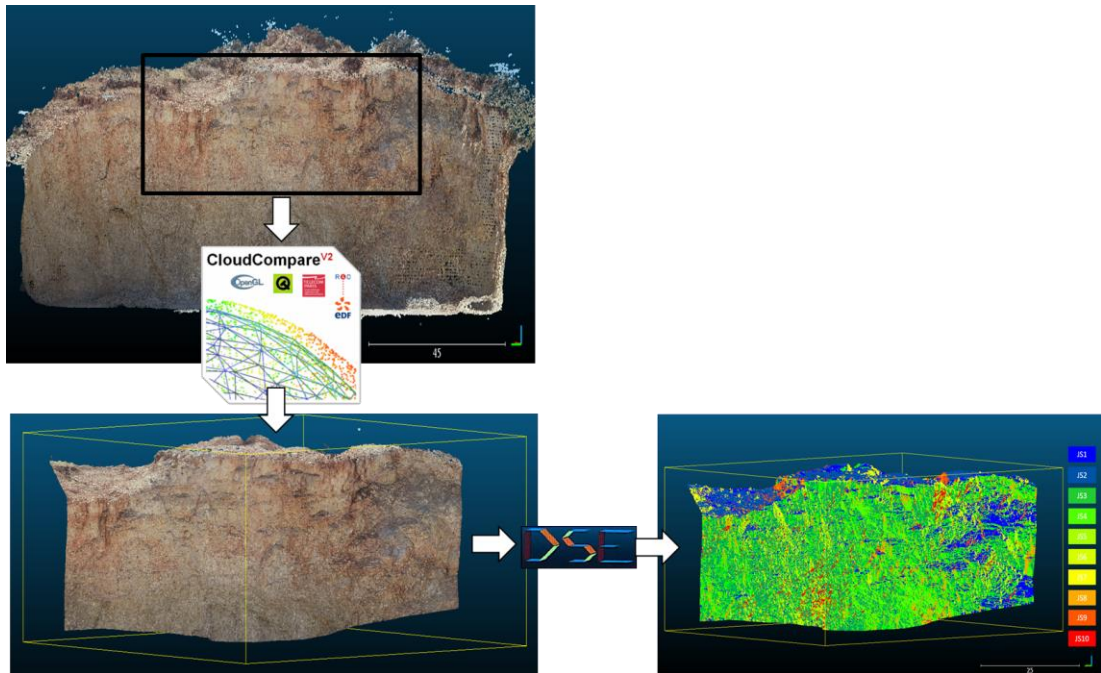


Figure 30: Critical Section of Quarry 3 clipped in CloudCompare

The statistical parameters used in the analysis are based on the optimal values suggested by the authors which has been verified on several steep slopes as discussed in section 2.4.2 Remote Sensing Techniques(Riquelme et al., 2014; Riquelme et al., 2017) and which shows efficient and accurate capture of the discontinuities and their orientation. These parameters were assigned as shown in Table 2.

Table 2: Statistical parameters used in DSE (Riquelme et al. (2014))

| Normal Vector Calculation | | Principal Poles Calculation | | Assignment of Points to a Principal Pole | Cluster Analysis |
|------------------------------------|------------------|-----------------------------|------------------------------------|---|-----------------------------------|
| Nearest Neighbours Coefficient knn | Tolerance η | Bins level | Min. angle between principal poles | Min. angle between normal of the principal planes | Min. number of points per cluster |
| 30 | 20% | 8 | 10° | 30° | 100 |

This method is not fully automated. It remains necessary for the operator to visually verify the detected discontinuity sets by placing them on the quarry face in CloudCompare. Figure 31 shows how the discontinuities in quarry face of Quarry 1 were extracted using DSE and viewed in CloudCompare to validate that the detected planes perfectly trace actual discontinuities. The length and spacing of the discontinuities were determined from either CloudCompare or ShapeMetriX software.

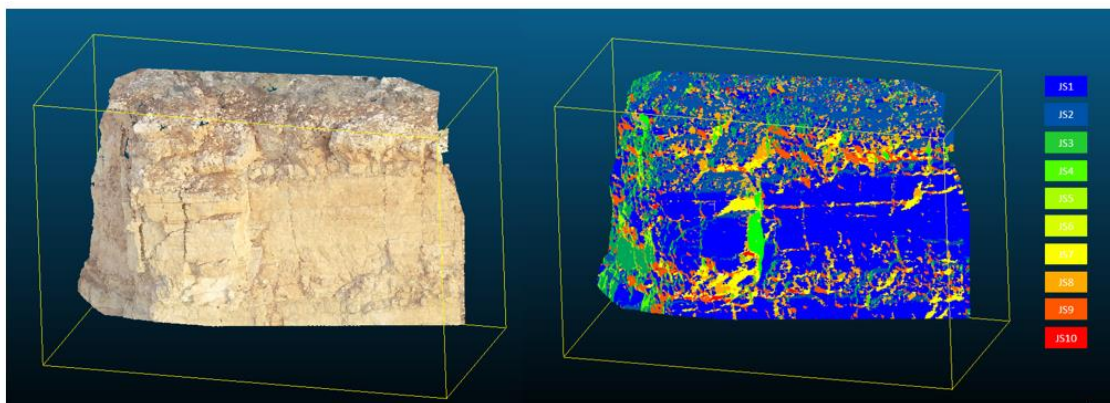


Figure 31: Overlaying DSE-detected joint sets on the quarry face in Quarry 1 using ClouCompare

3.5 Estimation of the Strength Parameters Along the Discontinuities

The scope of this research does not include field testing or sample extraction and thus the strength parameters were estimated based on the rock type and observations made on site and using the 3D models generated. For limestone rocks in Lebanon, we referred to the compressive strength determined in a study by Mrad et al. (2017) where a laboratory-based experimental work was performed on limestone rock cores collected from three different quarries in Lebanon located in the Beqaa region (the same zone of the four quarries selected for this study). The results showed that the unconfined compressive strength (UCS) of limestone ranged between 65 and 160 MPa, with a mean of 110 MPa. Moreover, they described limestone used for quarrying work as strong to very strong rock. Therefore, in this work, the UCS was set at 75 MPa and the joint compressive strength (JCS) was set at 50 MPa.

To estimate the shear strength along the discontinuity, Barton-Bandis criterion was adopted as discussed in section 2.3.1.2 Frictional Characteristics of Discontinuities. RocData software, a RocScience database of soil properties and models, was used where the JRC, JCS and rock residual friction angle ϕ_b were defined. For JRC, a visual comparison was made between the appearance of the discontinuity surface with the profiles shown in Figure 10. As for ϕ_b , two values, for dry and wet conditions, were selected to account for the friction reduction under rainfall events. The parameters considered are summarized in Table 3.

Table 3: Barton-Bandis strength parameters for the four quarries

| Location | Barton-Bandis criterion | | | |
|-------------|------------------------------------|-----|-----------------------------------|--|
| | Residual Friction Angle ϕ (°) | | Joint Roughness coefficient (JRC) | Joint Compressive strength (JCS) (MPa) |
| | Dry | Wet | | |
| Aarsal | 35 | 30 | 6 | 50 |
| Ain Bourday | 35 | 30 | 10 | 50 |
| Janta | 35 | 30 | 10 | 50 |
| Raiit | 35 | 30 | 10 | 50 |

3.6 Estimation of the Strength Parameters of the Rock Mass

For the general stability analysis, the rock mass was first classified based on the GSI classification system. The GSI value for each quarry was estimated by comparing the structure and surface conditions of the discontinuities with the chart shown in Figure 20. GSI was estimated as 55, 40, 45, and 65 for Quarry 1, 2, 3 and 4, respectively. Figure 32 shows a comparison of the GSI chart for jointed rocks and the slope face of Quarry 1. The comparison reveals that the slope surface appears to be “VERY BLOCKY” with “GOOD” quality due to the fact that the surface is rough and slightly weathered. Therefore, GSI 55 was assigned to Quarry 1.

The disturbance factor D was set to 1 for the first few meters (determined based on the heavily fractured part) of the top of the slope face and 0.7 for the remaining bottom part. This is because quarry blasting operations in Lebanon are uncontrollable and cause significant damage to the rock face near the crest of the slope. Then based on the selected GSI, UCS and D values, the Hoek-Brown rock mass strength parameters m , s , and a were suggested and tabulated in Table 4.



GEOLOGICAL STRENGTH INDEX FOR JOINTED ROCKS (Hoek and Martin, 2000)
 From the lithology, structure and surface conditions of the discontinuities, estimate the average value of GSI. Do not try to be too precise. Quoting a range from 31 to 37 is more realistic than stating that GSI = 35. Note that the table does not apply to structurally controlled failures. Where weak planar structural planes are present in an unfavourable orientation with respect to the excavation face, these will dominate the rock mass behavior. The shear strength of surfaces in rocks that are prone to deterioration as a result of changes in moisture content will be reduced if water is present. When working with rocks in the field in very poor conditions, a shift to the right may be made for wet conditions. Where pressure is dealt with by effective stress analysis.

| STRUCTURE | SUBFACE CONDITIONS | | SURFACE CONDITIONS | |
|---|--------------------|-----|--------------------|----|
| | 1 | 2 | 1 | 2 |
| INTACT OR MASSIVE – intact rock specimens or massive in situ rock with few widely spaced discontinuities | 90 | 85 | 90 | 85 |
| BLOCKY – well interlocked undisturbed rock mass consisting of cubical blocks formed by three intersecting discontinuity sets | 80 | 75 | 80 | 75 |
| VERY BLOCKY – interlocked, partially disturbed mass with multi-directional angular blocks formed by 3 intersecting sets | 70 | 65 | 70 | 65 |
| “BLOCKY OR SLURRY” – slabbed with angular blocks formed by many intersecting discontinuity sets. Persistence of bedding planes or schistosity | 60 | 55 | 60 | 55 |
| DISINTEGRATED – poorly interlocked, heavily broken rock mass with mixture of angular and rounded rock pieces | 50 | 45 | 50 | 45 |
| LAMINATED/SHEARED – lack of blockiness due to close spacing of weak schistosity or other planes | N/A | N/A | N/A | 10 |

Figure 32: GSI Selection for Quarry 1 based on Visual Comparison

Table 4: Hoek-Brown Parameters

| Location | Generalized Hoek-Brown Criterion | | | | | | |
|-------------|----------------------------------|-----|----|-----|------|--------|-------|
| | UCS (Intact rock) (MPa) | GSI | mi | D | mb | s | a |
| Aarsal | 75 | 55 | 10 | 0.7 | 0.84 | 0.0010 | 0.504 |
| Ain Bourday | 75 | 40 | 10 | 0.7 | 0.37 | 0.0002 | 0.511 |
| Janta | 75 | 50 | 10 | 0.7 | 0.84 | 0.0010 | 0.504 |
| Raiit | 75 | 65 | 10 | 0.7 | 1.46 | 0.0060 | 0.502 |

3.7 Kinematic Analysis

Kinematic analyses were performed in DIPS software by RocScience to determine the likelihood of failure and its types (planar, wedge and toppling). A pole plot was created using equal angle projection to represent the orientation of discontinuities extracted previously using DSE and the slope dip and dip direction were then defined. The friction angle was set to 30° corresponding to the residual wet friction angle of limestone to be considered for the worst-case scenario. For the analysis of planar and wedge failures, a lateral limit of 20° was used (Hudson & Harrison, 1997; Sivakugan et al., 2013). As for toppling analysis, it was set to 30° (Goodman, 1980).

3.8 Analysis of Structurally Controlled Failures using Limit Equilibrium methods

Based on the type of failure identified using previous kinematic analysis, mode-specific software by RocScience were used to determine the factor of safety based on limit equilibrium methods under dry, rain, and seismic conditions. Slopes susceptible to planar failure were assessed using RocPlane, while those at risk of wedge failure or toppling failure were evaluated using SWedge and RocTopple, respectively.

The input data for the three software are mainly the slope height, dip, and dip direction as well as the orientation of the discontinuities kinematically found to be at risk of failure. In addition, Barton-Bandis joint strength parameters were used in the analysis to estimate the strength along the discontinuities. For RocPlane and SWedge software, and in order to limit the size of the wedge formed by certain combinations that have an unrealistic size and extension, the bench width and the length of the slope (Figure 33) were assumed to be 10 meters and 30 meters, respectively. Moreover, the minimum wedge size was set to 1kN to filter out very small insignificant wedges. As for RocTopple software, the input parameters were not elaborated since no toppling failure was identified and thus the software was not used.

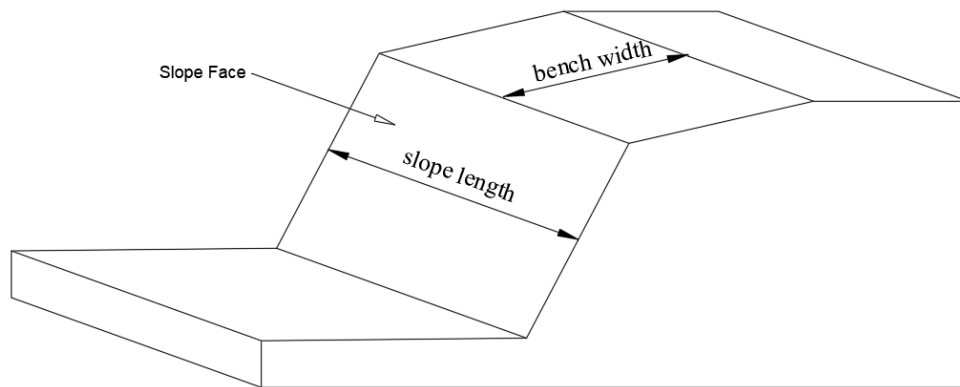


Figure 33: Slope length and bench width

3.9 Analysis of Non- Structurally Controlled Failures using Limit Equilibrium methods

As discussed earlier, this analysis is often used for preliminary assessment of the engineering behaviors of the rock mass. The stability of the overall slope face was assessed since the quarries showed in certain parts close-spaced joint. The two-dimensional limit equilibrium analysis (2D LEA) software Slide2 by RocScience was used. 2D cross-sections showing the critical slope height and heavily fractured rock mass were extracted from the 3D quarry model as shown in Figure 34. Each section was then imported into Slide2 and evaluated by adopting cuckoo search optimized slip surface in Janbu and Bishop methods for slope safety factor determination. For shear strength parameters, the generalized Hoek-Brown criterion for intact rock and rock mass as defined in the previous section was used. The assessment of the slope under rainfall events was modeled by setting the level of the groundwater table based on the percentage of saturation determined using the Average Annual Rainfall map (Plassard, 1971). For example, if the saturation level is found to be 17%, then the groundwater table has risen to a level of 17% of the slope height. As for seismic stability analysis,

the horizontal seismic load coefficient was set to equal to the PGA chosen from the PSHA map of Lebanon (Huijer et al., 2011).

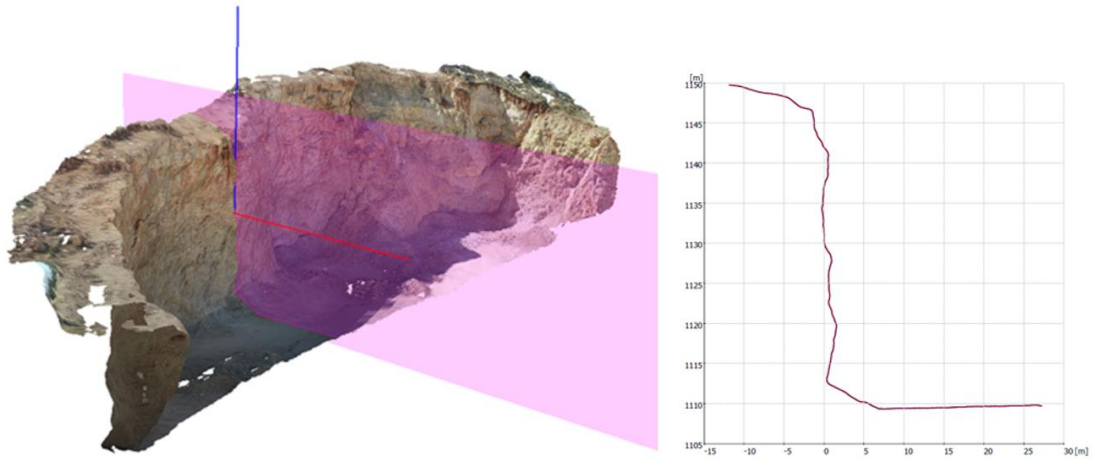


Figure 34: 2D cross-section extraction from 3D Model of Quarry 3

3.10 Runout Distance and Angle of Reach

RocFall software by RocScience was selected to perform a probabilistic trajectory analysis to assess the hazard posed by the detachment of the rock blocks from the slope surface. The lumped mass approach and rigid body approach are two possible options distinguished by the way the rock mass is represented in the model. The first model considers the rock block as a dimensionless point, while the second model considers the geometry of the rock block in the rockfall simulations. The latter is more reliable and allows for the design of more conservative protection measures (Dadashzadeh, 2014) and was therefore adopted in this study. The weights and dimensions of the rock blocks were obtained from the 3D model constructed using the volume calculation option of the blocks showing risk of failure. Release points called seeders were positioned at the highest point of the slope in order to generate the highest potential energy and therefore the highest runout distance. The total number of blocks released from the seeders was assumed to be 1000 since the software employs a probabilistic

analysis to determine the runout distance with different probability of occurrence. The initial conditions of these blocks were kept as default, i.e., zero linear and angular initial velocity as they slide in free fall. The model calculates the runout distance by computing the conversion of potential energy into kinematic energy considering the energy loss due to friction and due to inelastic deformation during the collision of a rock with the slope or bench. Thus, the coefficients of restitution (R) defined in the normal direction and tangential to the slope and dynamic and rolling friction coefficients were assigned as shown in Table 5 and were assumed to follow a normal distribution because the analysis is very sensitive to the value of these parameters. Slope face and ground surface properties were defined by the same parameters of a limestone face as in Azzoni et al. (1995) and Robotham et al. (1995), although in some areas of the same quarry, the ground surface was composed of crushed limestone which has lower friction and restitution coefficients resulting in a lower runout distance.

Table 5: Summary of coefficient of restitution and friction coefficients used for rockfall analysis

| Terrain Type | R_n | R_t | Dynamic Friction | Rolling Friction |
|--|----------------------------------|----------------------------------|--------------------------|-------------------------|
| Limestone face & Ground Surface | Mean: 0.315 Std Dev: 0.064 | Mean: 0.712 Std Dev: 0.116 | Mean: 0.57 Std Dev: 0 | Mean: 0.4 Std Dev: 0 |

Chapter Four

Interpretation of Results

This chapter presents the results of the various steps performed to assess the stability of the quarry faces. Slope classification, discontinuities, and rockfall potential are addressed in the following sections for the four selected quarries.

4.1 Digital Elevation Model (DEM) of the Four Quarries Mapped using UAV

Figure 35 shows the DEMs of the four quarries created in CloudCompare using the generated 3D point cloud file. It is clear that the slope face in all these quarries is very steep through the change of colours, indicating a significant decrease in height along a short horizontal distance. This is consistent with what was observed during the site visits, and from the satellite images produced using Google Earth (Figure 36). All quarry faces have near vertical cuts.

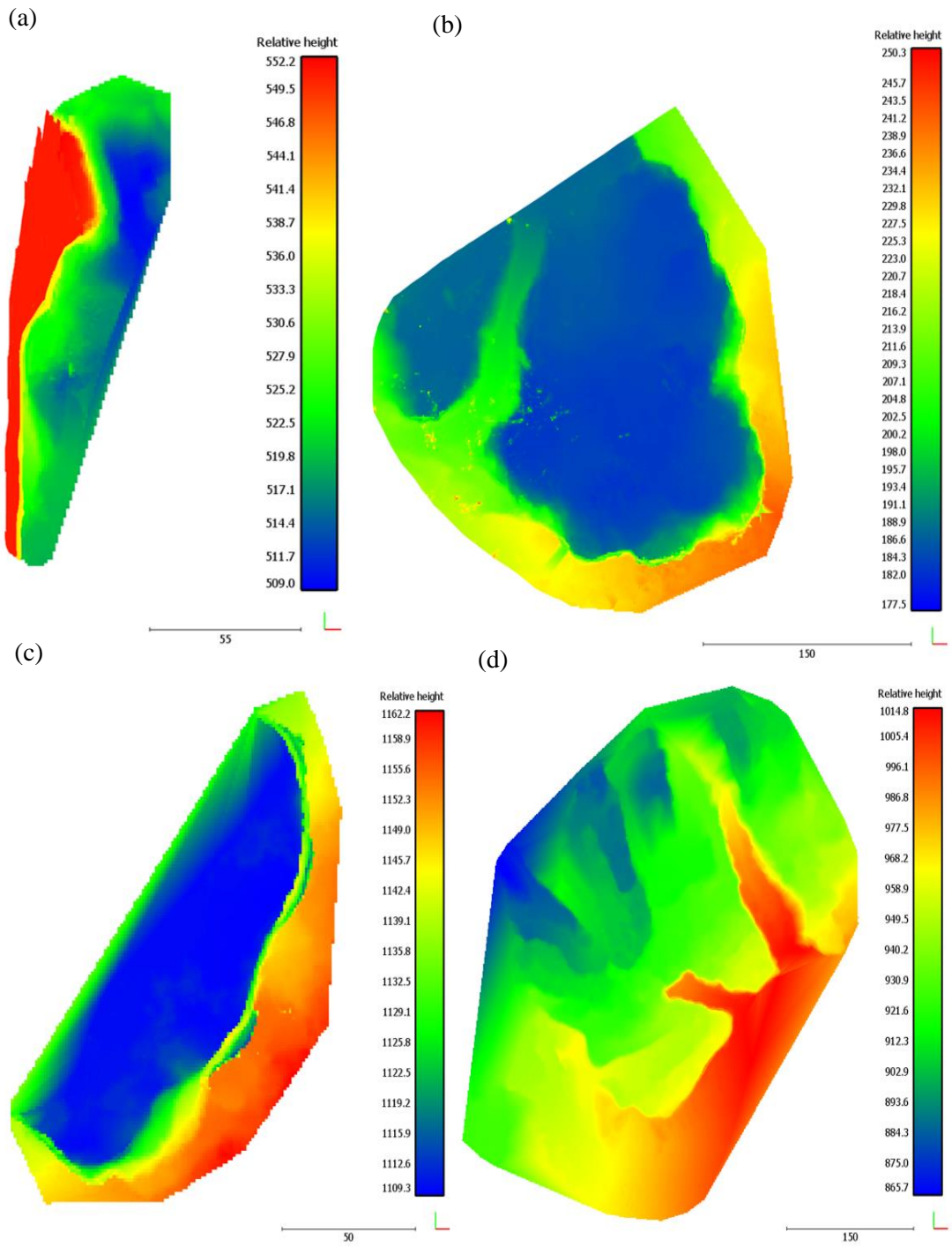


Figure 35: DEM of a) Quarry 1, b) Quarry 2, c) Quarry 3, and d) Quarry 4



Figure 36: Satellite Image of the four quarry sites reproduced using Google Earth

4.2 Discontinuity Orientation Extraction

The statistical analysis from point clouds using DSE allowed the identification of ten discontinuity sets (DS) per quarry face as shown in Figure 37. Table 6 illustrates the orientations of these sets (dip and dip direction).

Table 6: Discontinuity sets extracted from the point clouds

| Location | Joint Set | 1 | 2 | 3 | 4 | 5 | 6 | 7 | 8 | 9 | 10 |
|-------------|------------------------------|-----|-----|-----|-----|-----|-----|-----|-----|-----|-----|
| Aarsal | Dip ($^{\circ}$) | 85 | 19 | 73 | 79 | 62 | 87 | 78 | 63 | 82 | 43 |
| | Dip Direction ($^{\circ}$) | 84 | 88 | 129 | 5 | 165 | 331 | 239 | 48 | 286 | 232 |
| Ain Bourday | Dip ($^{\circ}$) | 78 | 11 | 57 | 79 | 36 | 81 | 79 | 70 | 69 | 79 |
| | Dip Direction ($^{\circ}$) | 191 | 305 | 215 | 240 | 254 | 85 | 34 | 2 | 273 | 158 |
| Janta | Dip ($^{\circ}$) | 44 | 12 | 83 | 73 | 73 | 85 | 39 | 80 | 41 | 66 |
| | Dip Direction ($^{\circ}$) | 314 | 306 | 120 | 320 | 151 | 271 | 256 | 352 | 10 | 78 |
| Raiit | Dip ($^{\circ}$) | 85 | 39 | 14 | 57 | 19 | 56 | 88 | 31 | 50 | 48 |
| | Dip Direction ($^{\circ}$) | 237 | 250 | 327 | 215 | 182 | 285 | 267 | 106 | 178 | 327 |

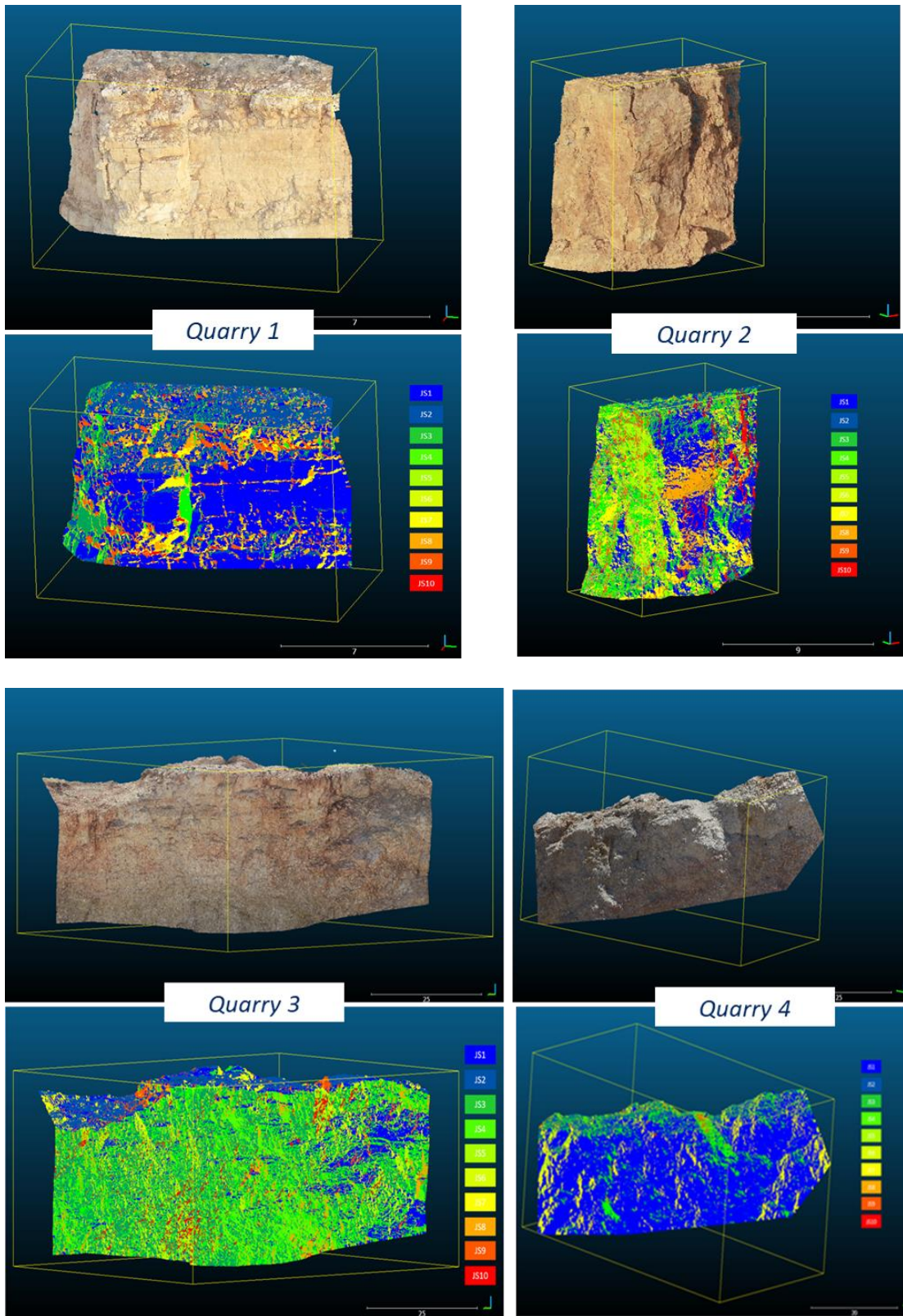


Figure 37: The color scale represents the discontinuity sets assigned to each point of the critical face that was cropped from each quarry face.

To verify the plane identification with DSE, the results are compared with the mapping results from ShapeMetriX3D. For instance, for Quarry 3, JS7 (dip = 39° and dip direction = 256°) was detected using DSE and is shown in Figure 38b. The orientation of the same discontinuity set was then determined using ShapeMetriX3D by drawing a plane along the discontinuity (Figure 38a) and was found to have a dip and dip direction of 40° and 255° , respectively. This shows that both methods give the same results, and that the statistical analysis is verified to be able to perfectly detect

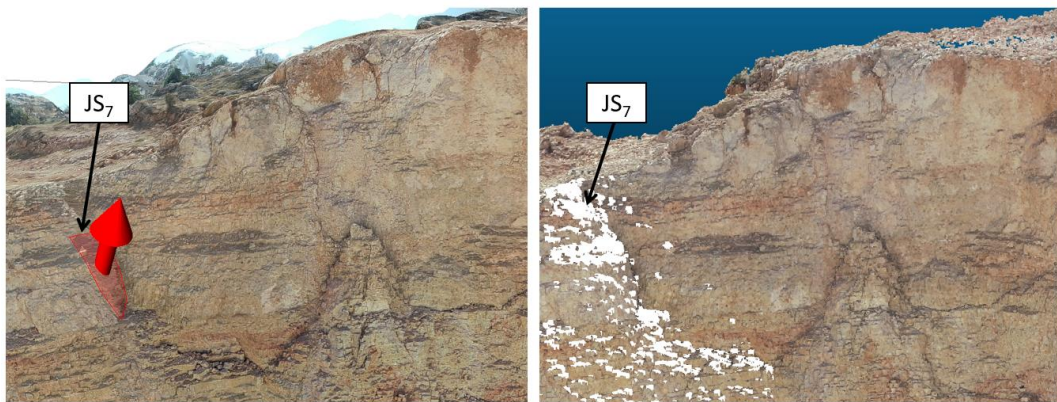


Figure 38: The orientation of JS7 (from Quarry 3) obtained with b) DSE, was verified using a) ShapeMetrix software.

4.3 Kinematic Analysis of Quarry Faces

The results of the kinematic analysis will be discussed in this section for each failure mode separately.

4.3.1 Planar Failure

For Quarry 1, Quarry 2, and Quarry 3, none of the detected poles fall within the critical zone for planar sliding (Figure 40a, Figure 40b, and Figure 40c) indicating that there is no potential for planar failure.

As for Quarry 4, JS2 and JS4 fall within this zone (Figure 40d) and thus the slope shows a 23% probability of planar failure. This is confirmed by inspecting the 3D

model as the orientation of JS2, for example, is dipping out of the slope face showing the possibility of the block sliding along this discontinuity (Figure 39).

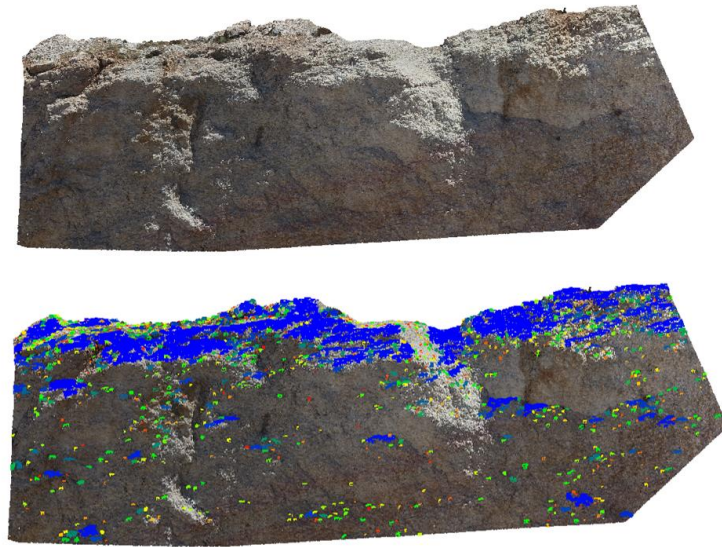


Figure 39: JS2 in Quarry 4 shows a risk of planar sliding

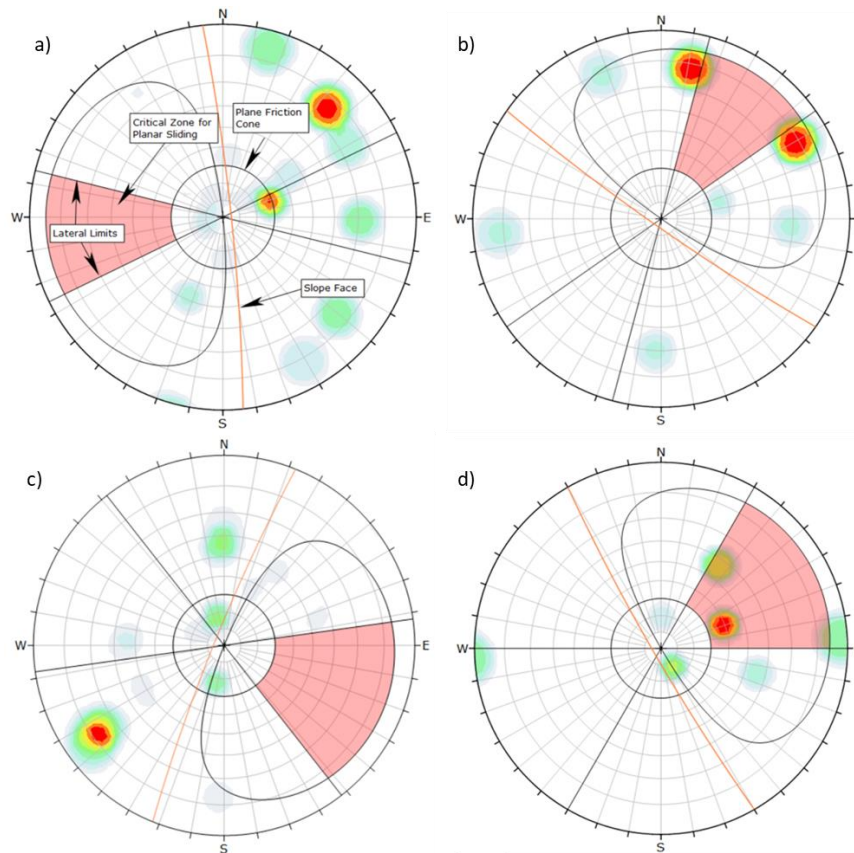


Figure 40: Kinematic analysis of planar failure using DIPS on a) Quarry 1, b) Quarry 2, c) Quarry 3, and d) Quarry 4

4.3.2 Wedge Failure

The result of the kinematic analysis shows that the probability of wedge sliding is 29%, 63%, 44%, and 53% for Quarry 1, Quarry 2, Quarry 3, and Quarry 4, respectively. This highlights that the wedge failure has high probability of occurrence for the four quarries selected. Figure 41 shows the stereographic projection of all discontinuity planes intersection and those falling in the crescent shaped critical area are considered vulnerable to wedge sliding.

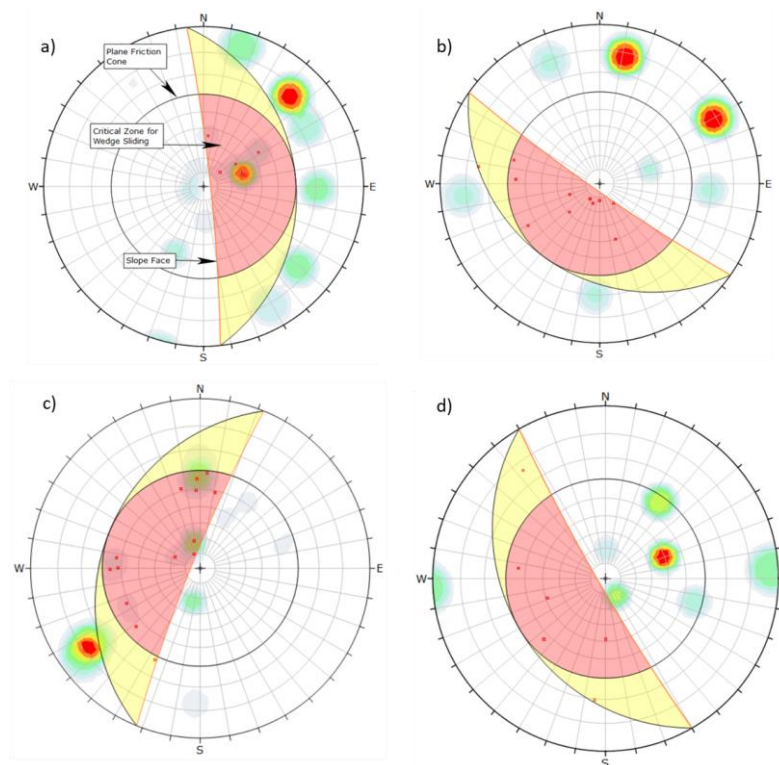


Figure 41: Kinematic analysis of wedge failure using DIPS on a) Quarry 1, b) Quarry 2, c) Quarry 3, and d) Quarry 4

For Quarry 1, JS3 and JS8 meet inside the slope to form an unstable wedge block as shown in Figure 42. Similarly, Figure 43 shows two discontinuity sets (JS1 and JS4) in Quarry 2 intersecting to form a rock wedge sandwiched between two planes having the potential to slide in the direction of the line of intersection. For Quarry 3, the wedge block formed by JS4 and JS7 is massive compared to other quarries where blocks are formed at the crest of the slope (Figure 44). The area of this block face was calculated

in CloudCompare and was determined to be 550 m². As for Quarry 4, JS4 and JS5 also shows a risk of wedge sliding (Figure 45).

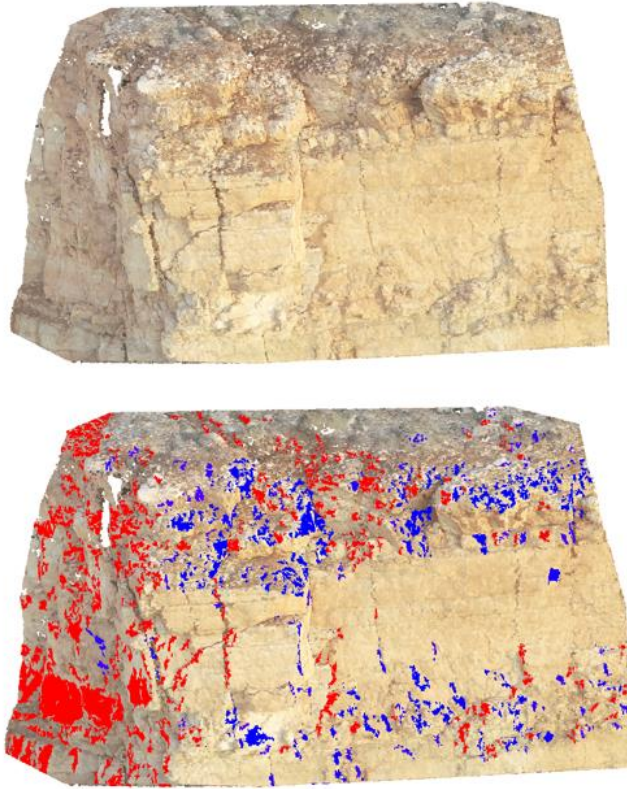


Figure 42: JS3 and JS8 showing a risk of wedge sliding (Quarry 1)

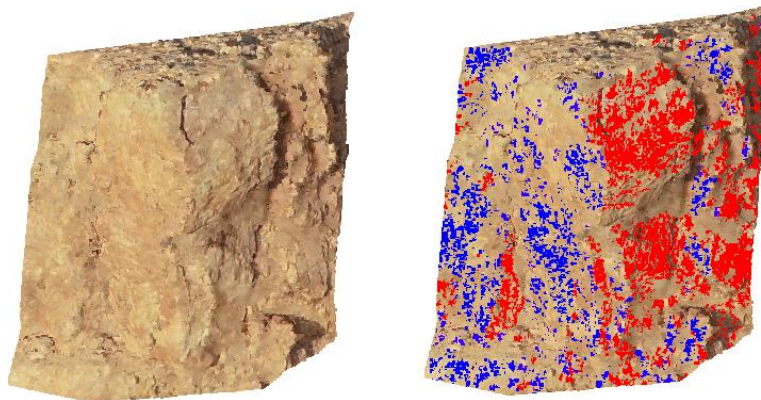


Figure 43: JS1 and JS4 showing a risk of wedge sliding (Quarry 2)

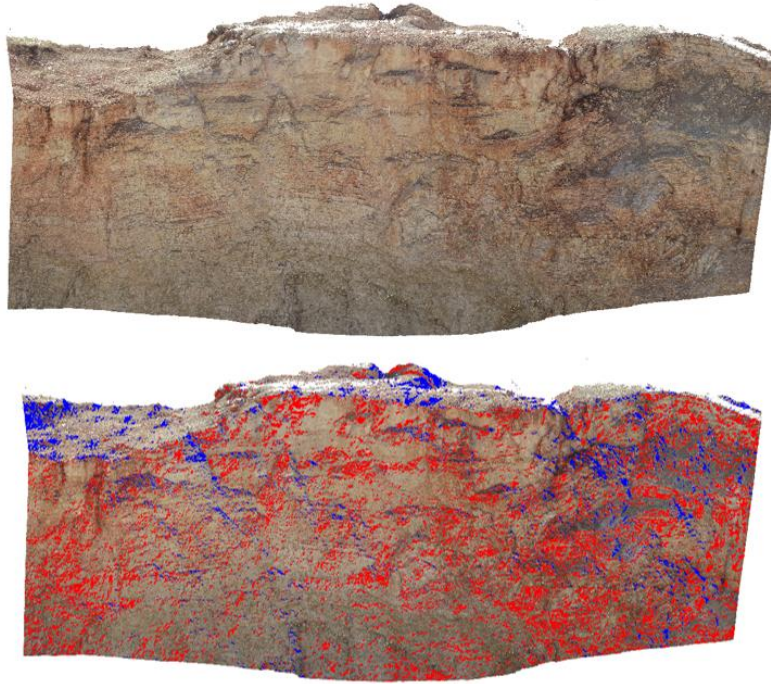


Figure 44: JS4 and JS7 showing a risk of wedge sliding (Quarry 3)

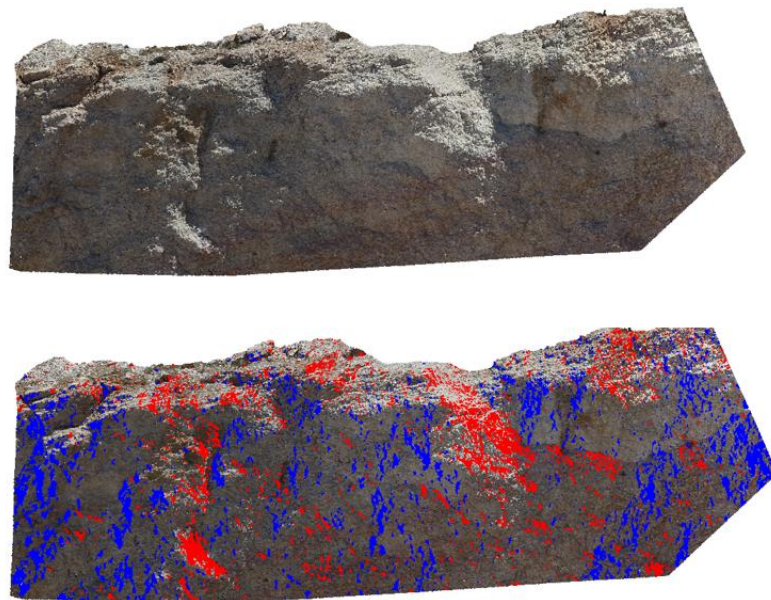


Figure 45: JS4 and JS7 showing a risk of wedge sliding (Quarry 4)

4.3.3 Toppling Failure

Based on the results of the kinematic analysis shown in Figure 46, it was found that the conditions for toppling failure to occur were not fulfilled in any of the selected quarries. In fact, toppling failure occurs in typical geological conditions where steeply dipping discontinuities separate continuous columns of rock, putting them at risk of bending. Since these conditions are not present in the analyzed quarries, it explains why this mode is unlikely to occur in quarry slopes (zero-probability).

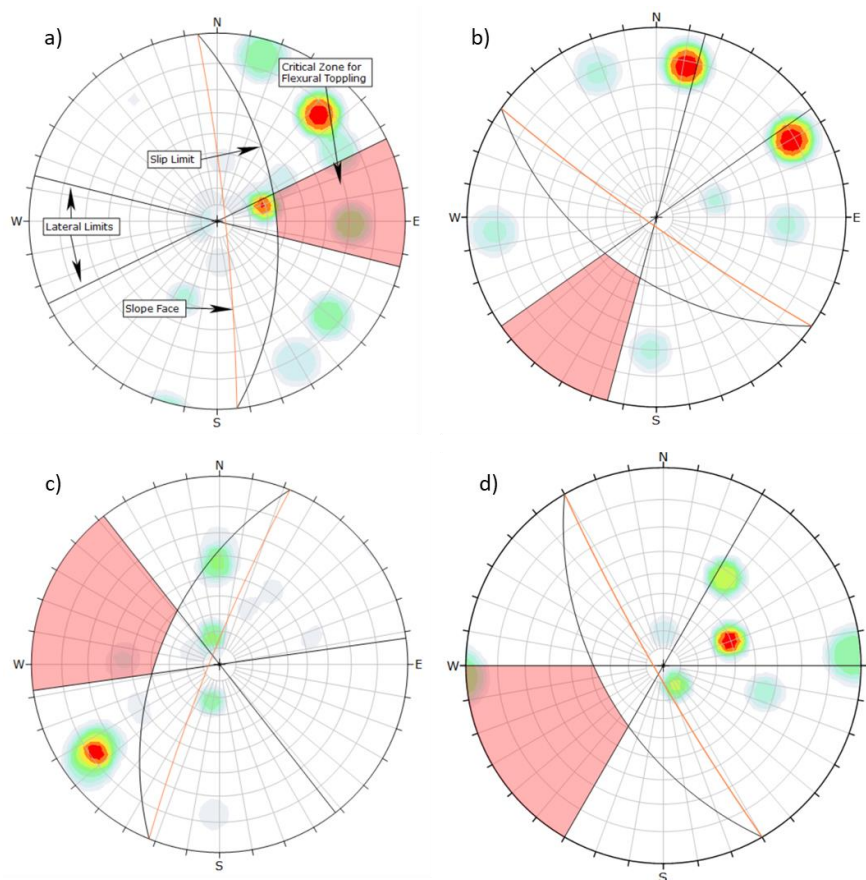


Figure 46: Kinematic analysis of flexural toppling using DIPS on a) Quarry 1, b) Quarry 2, c) Quarry 3, and d) Quarry 4

4.4 Dominant Mode of Failure

To determine the probability of each failure mode at limestone quarry sites, the results of the kinematic analyses performed in this research as well as those of Kaafarani (2019) research were considered since in her work, a limestone quarry was also

assessed using the same methodology adopted here. The findings of both works are summarized in Table 7.

Table 7: Probability of failure modes for each quarry sites

| Location | Probability (%) | | |
|---------------------------------|-----------------|-------|----------|
| | Planar | Wedge | Toppling |
| Aarsal | 0 | 29 | 0 |
| Ain Bourday | 0 | 63 | 0 |
| Janta | 0 | 44 | 3 |
| Raiit | 23 | 53 | 0 |
| Baflie (kaafarani, 2020) | 22 | 46 | 22 |

The total probability theorem is applied to extrapolate the findings of the two studies on limestone quarries in Lebanon in general. In fact, the 29% probability of wedge failure in Aarsal quarry represents the probability of this wedge failure **given** that the selected quarry is located in the Aarsal site. It is represented by the following:

P (wedge failure/Aarsal quarry)

In order to determine the probability of wedge failure for any randomly selected limestone quarry in Lebanon, the total probability should be computed by summing the individual probabilities from each contributing part.

$$P(A) = \sum_{i=1}^n P(A \cap X_i) = \sum_{i=1}^n P(A/X_i) P(X_i)$$

Therefore, the probability of wedge failure is calculated as follows:

$$\begin{aligned} P(\text{Wedge failure}) &= P(W) \\ &= P(W/Q_1) P(Q_1) + P(W/Q_2) P(Q_2) + P(W/Q_3) P(Q_3) \\ &\quad + P(W/Q_4) P(Q_4) + P(W/Q_5) P(Q_5) \end{aligned}$$

where $P(Q_1) = P(Q_2) = P(Q_3) = P(Q_4) = P(Q_5) = \frac{1}{n} = \frac{1}{5}$ and the conditional probabilities $P(W/Q_i)$ are those computed in this study and shown in Table 7.

Table 8: Total probability of the three failure modes

| | Planar | Wedge | Toppling |
|--------------------|---------------|--------------|-----------------|
| Probability | 9% | 47% | 5% |

The total probability of the three failure modes is summarized in Table 8. It highlights that wedge sliding is the most likely mode of failure for near vertical limestone quarry slope with a 47% probability of occurrence while planar and toppling failures are relatively unlikely. These results confirm the observations of Wyllie (2015) that plane failure is a comparatively rare sight in rock slopes because it is only occasionally that all the geometric conditions required to produce such a failure occur in an actual slope, whereas wedge failures can occur over a much wider range of geologic and geometric conditions than plane failures. Regarding toppling failure, it occurs in typical geological conditions where the discontinuities are near vertical forming continuous columns of rock which are unusual for limestone quarry slopes (Hudson & Harrison, 1997; Sivakugan et al., 2013). These conditions were not met in any of the quarries analyzed.

4.5 Stability Analysis of the Quarry Faces Based on Limit Equilibrium Methods

In this section, the results of limit equilibrium analyses on the joint sets that were found to be kinematically unstable in section will be presented. RocPlane and SWedge programs were used to perform planar and wedge rock slope stability analysis, respectively. The analysis was performed using the deterministic analysis that derives safety factors for a particular geotechnical situation. If the factor of safety is less than

1.3 (Hoek et al., 1981), the quarry is considered unstable and should be evaluated in RocFall to determine the runout distance.

4.5.1 RocPlane Results

The safety factors of the analyzed joint sets are summarized in Table 9. Cases highlighted in black indicate definite planar failures. Figure 47 and Figure 48 show an example of the 3D and 2D models of JS2 in Quarry 4 (Figure 39), respectively, analyzed in RocPlane.

Table 9: Factors of safety determined from RocPlane under dry and wet conditions, as well as seismic loading

| Location | Joint Set | F.S (Dry Conditions) | F.S (Wet Conditions) | F.S (Seismic Loading) |
|----------|-----------|----------------------|----------------------|-----------------------|
| Raiit | JS2 | 2.24 | 2.21 | 1.42 |
| | JS4 | 1.56 | 1.42 | 1.03 |

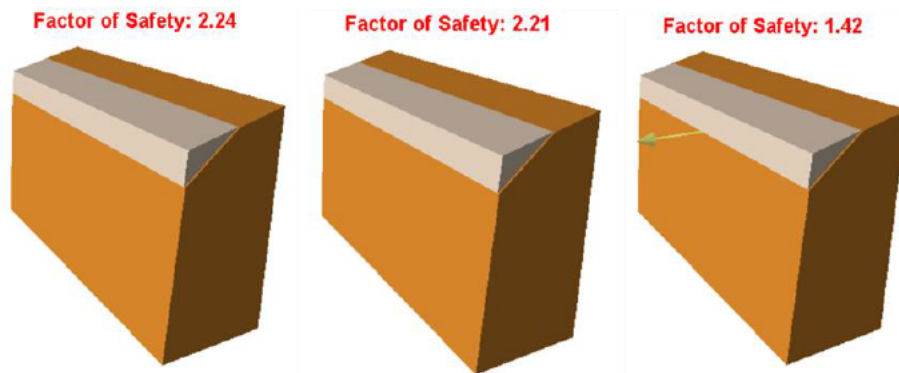


Figure 47: Factor of safety of JS2 of Quarry 4 under (a) Dry conditions (b) Wet conditions (c) Seismic loading

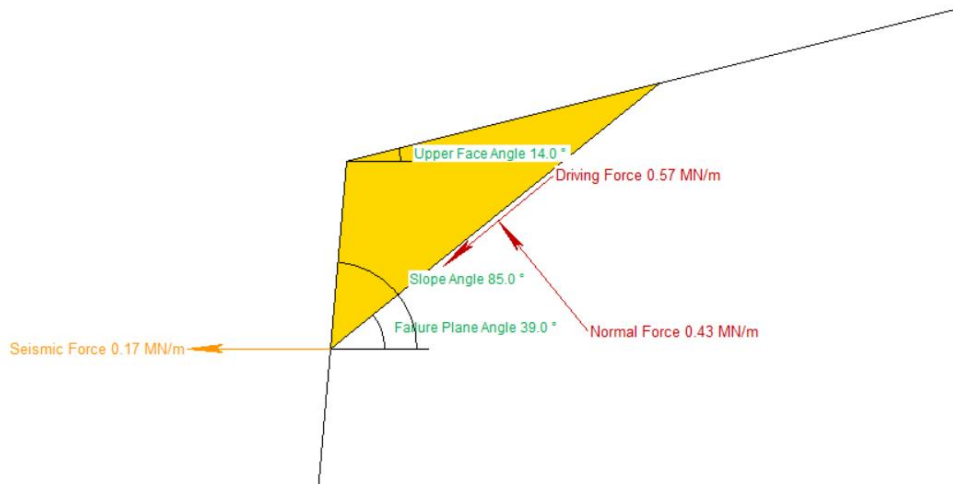


Figure 48: 2D view of the JS2 model showing the applied and resultant forces under seismic event.

4.5.2 SWedge Results

Similarly, the safety factors of the analyzed joint set interactions are summarized in Table 10. Cases highlighted in black indicate definite wedge failures. Figure 49 shows an example of the 3D models of the intersection of JS4 and JS7 in Quarry 3 (Figure 44) analyzed in SWedge.

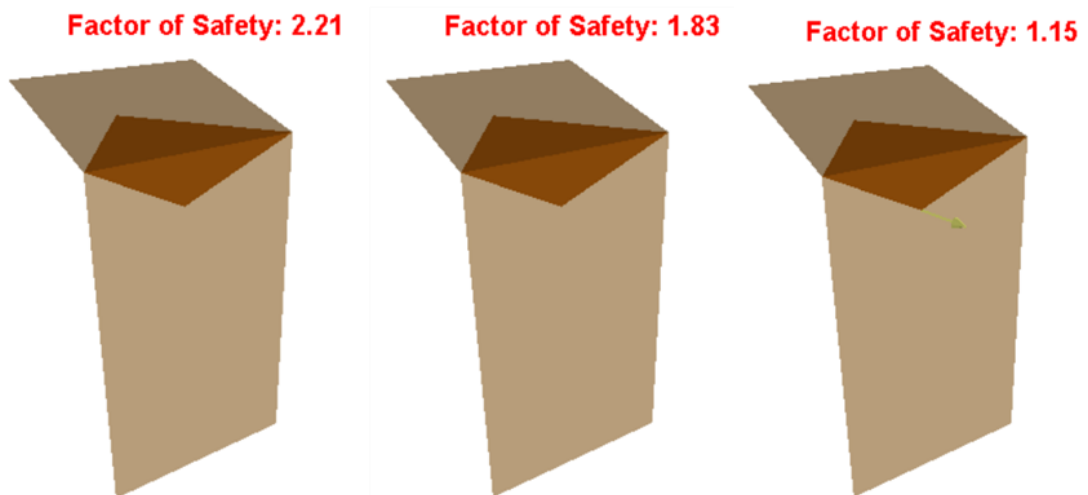


Figure 49: Factor of safety of wedge formed by JS1 and JS7 in Quarry 3 under (a) Dry conditions (b) Wet conditions (c) Seismic loading

Table 10: Factors of safety determined from SWedge under dry and wet conditions, as well as seismic loading

| Location | Joint Set Intersections | | F.S (Dry Conditions) | F.S (Wet Conditions) | F.S (Seismic Loading) |
|--------------------|-------------------------|------|----------------------|----------------------|-----------------------|
| Aarsal | JS4 | JS8 | 1.47 | 1.21 | 0.95 |
| | JS4 | JS6 | 1.48 | 1.26 | 0.73 |
| | JS4 | JS3 | 1.53 | 1.36 | 1 |
| | JS8 | JS3 | 1.62 | 1.41 | 1.31 |
| | JS6 | JS3 | 4.98 | 4.15 | 3.55 |
| Ain Bourday | JS1 | JS4 | 1.32 | 1.3 | 0.67 |
| | JS1 | JS9 | 1.57 | 1.5 | 0.88 |
| | JS1 | JS5 | 3.21 | 3.2 | 2.23 |
| | JS1 | JS6 | 1.31 | 1.23 | 0.54 |
| | JS1 | JS10 | 1.5 | 1.43 | 0.94 |
| | JS10 | JS5 | 3.61 | 2.89 | 2.47 |
| | JS10 | JS9 | 1.98 | 1.8 | 1.25 |
| | JS3 | JS4 | 16.24 | 16.2 | 10.82 |
| | JS3 | JS6 | 5.56 | 5.55 | 3.87 |
| | JS3 | JS5 | 1.82 | 1.78 | 1.5 |
| | JS3 | JS8 | 1.81 | 1.77 | 1.42 |
| | JS8 | JS5 | 3.79 | 3.03 | 2.66 |
| | Ain Bourday | JS6 | JS1 | 2.55 | 2.02 |
| JS6 | | JS9 | 1.98 | 1.64 | 1.36 |
| JS7 | | JS4 | 2.95 | 2.44 | 2 |
| JS1 | | JS7 | 2.34 | 1.93 | 1.6 |
| JS1 | | JS8 | 4.57 | 3.79 | 3.11 |
| JS1 | | JS10 | 1.45 | 1.21 | 1.12 |
| JS9 | | JS10 | 2.05 | 1.68 | 1.41 |
| JS8 | | JS4 | 1.31 | 1.09 | 0.55 |
| JS8 | | JS1 | 4.57 | 3.79 | 3.11 |
| JS8 | | JS7 | 2.42 | 2 | 1.65 |
| Raiit | JS4 | JS7 | 1.78 | 1.43 | 1.2 |
| | JS4 | JS6 | 2.52 | 2.07 | 1.64 |
| | JS4 | JS2 | 3.39 | 3.2 | 2.36 |
| | JS6 | JS2 | 7.35 | 6.43 | 4.93 |

Based on the results obtained, none of the quarries showed any risk of failure under dry condition which was confirmed by the observations made on site, as no failure was detected. As for wet conditions, the safety factors are slightly lower than in dry condition because limestone is considered relatively impermeable with water occupying 16 to 17% of the joint height, which slightly decreases the friction between joint asperities as well as the effective stress, which therefore reduce the factor of

safety. However, for the seismic loading, the safety factors decrease significantly since the seismic coefficient was assumed equal to the PGA which is considered relatively high (PGA is 0.225 for Quarry 1 and 0.25 for Quarries 2, 3, and 4). The limit equilibrium programs (RocPlane and SWedge) perform the analysis by applying a horizontal seismic force equal to the product of the seismic coefficient, the acceleration due to gravity ($g = 9.81 \text{ m/s}^2$), and the mass of the sliding block.

4.6 Stability Analysis Results for Non-Structurally Controlled Failure Based on Limit Equilibrium Methods

All the results of the general slope stability analysis are described in Table 11 and shown in Figure 50 to Figure 53. The present study shows that the four quarries are stable in terms of general slope and thus the overall stability of slope is not a problem in limestone quarries. These results are consistent with the assertion of El Fadel et al. (2001) that for most of the quarry sites in Lebanon, the overall geological stability is considered adequate due to the nature of the rock and favorable geological conditions. In addition, Wyllie (2015) stated that for most rock cuts whose slopes are less than 100 m (300 ft) in height, the stresses in the rock are much less than the rock strength so that fracturing of intact rock is unlikely.

Table 11: Factors of safety determined from Slide2 under dry and wet conditions, as well as seismic loading

| Location | F.S (Dry Conditions) | F.S (Wet Conditions) | F.S (Seismic Loading) |
|--------------------|-----------------------------|-----------------------------|------------------------------|
| Aarsal | 4.22 | 4.15 | 3.15 |
| Ain Bourday | 2.41 | 2.29 | 2.19 |
| Janta | 2.63 | 2.6 | 2.28 |
| Raiit | 2.59 | 2.37 | 2.19 |

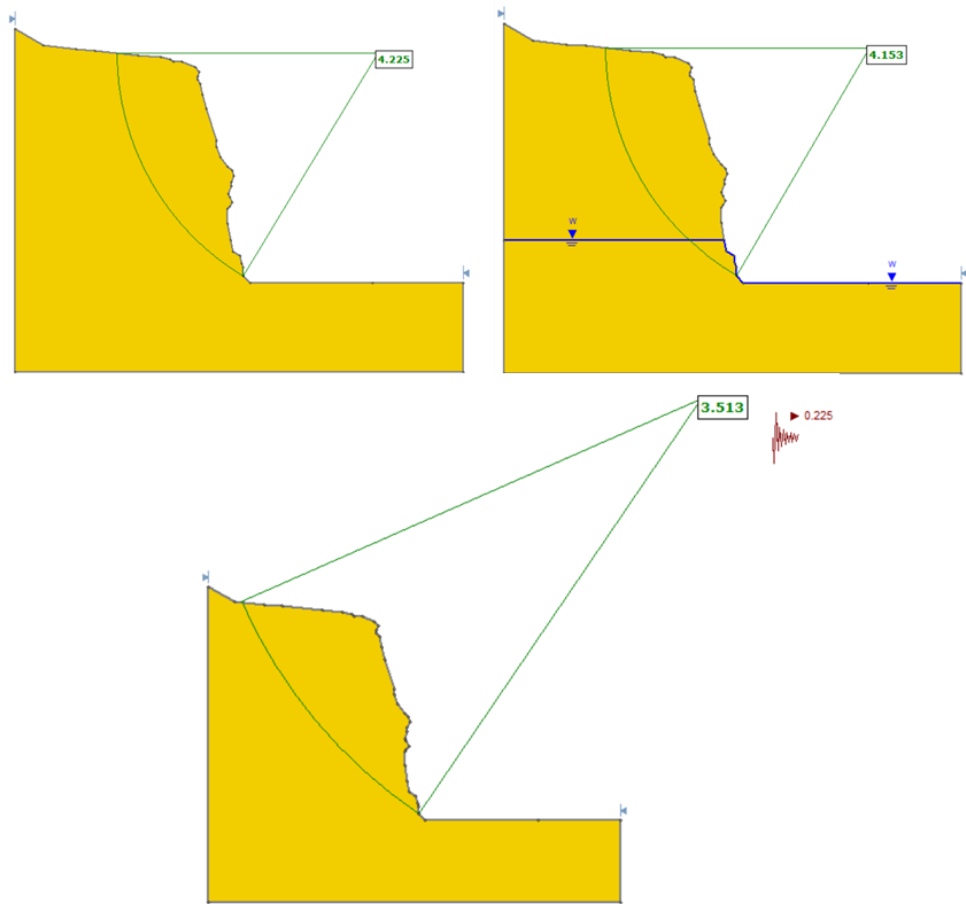


Figure 50: Factor of safety of the overall slope in Quarry 1 under (a) Dry conditions (b) Wet conditions (c) Seismic loading

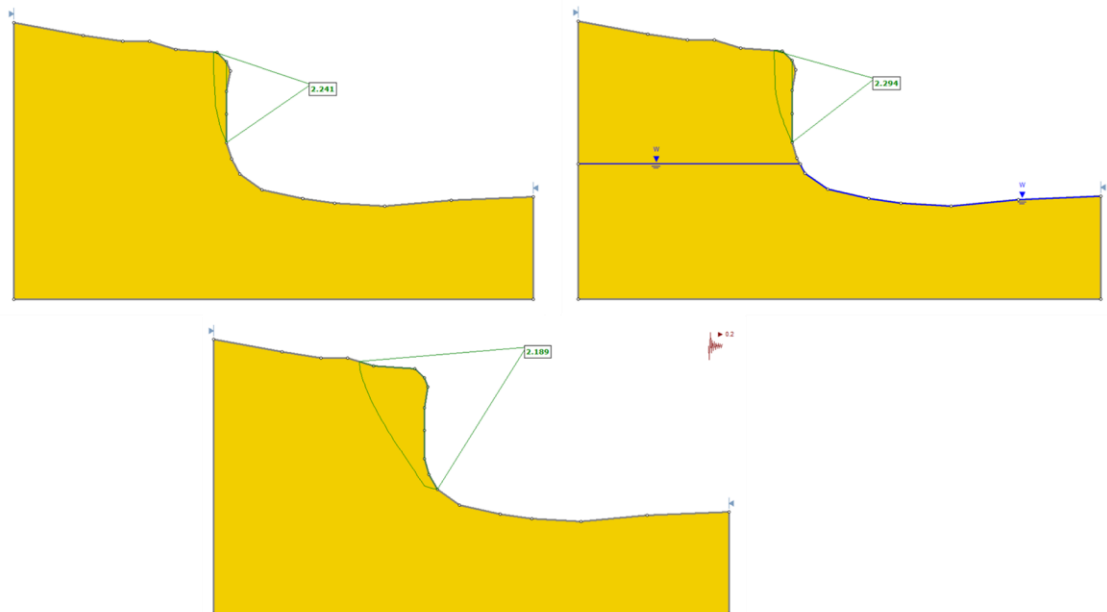


Figure 51: Overall Slope Stability Results for Quarry 2 under (a) Dry conditions (b) Wet conditions (c) Seismic loading

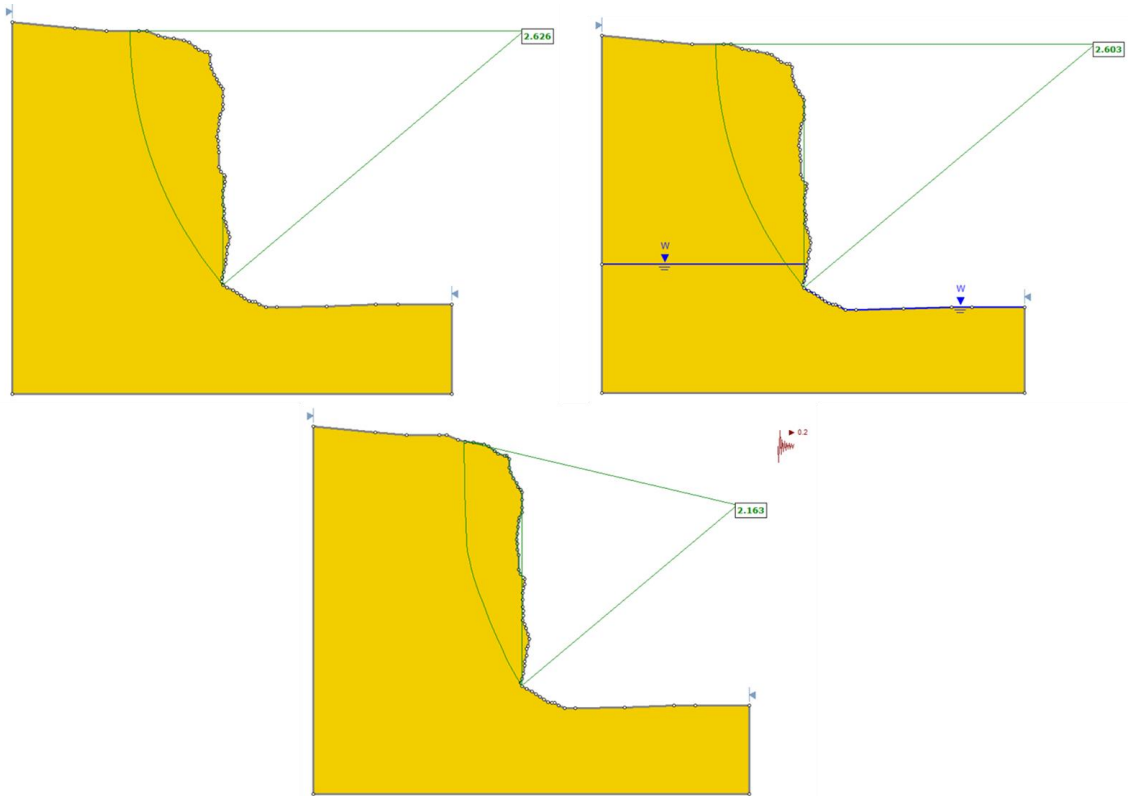


Figure 52: Overall Slope Stability Results for Quarry 3 under (a) Dry conditions (b) Wet conditions (c) Seismic loading

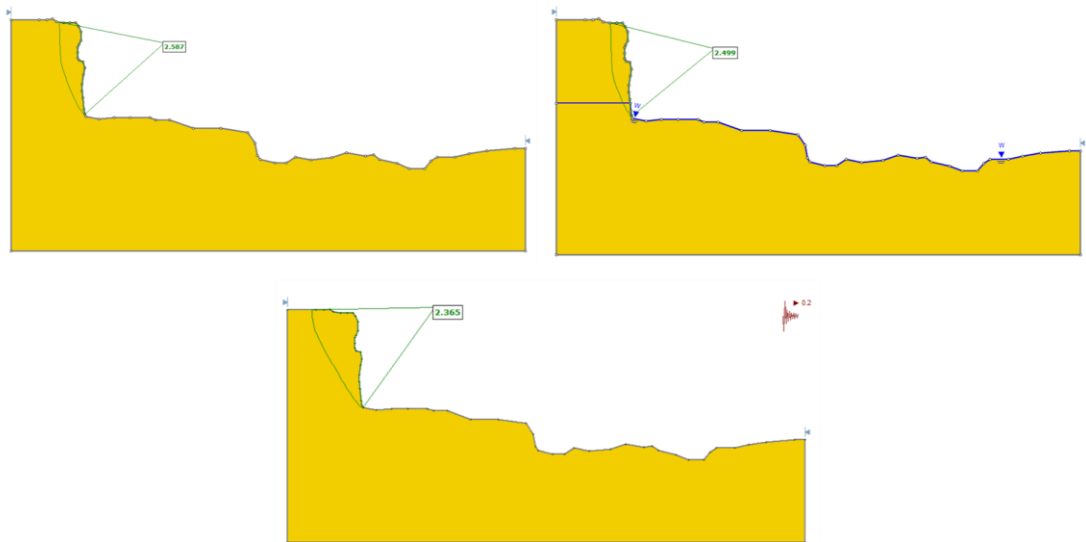


Figure 53: Overall Slope Stability Results for Quarry 4 under (a) Dry conditions (b) Wet conditions (c) Seismic loading

4.7 Maximum Runout Distance and Angle of Reach

Since RocFall assess slopes at risk of rockfalls based on a statistical analysis, a distribution of rock fall path end locations is obtained for each trial computed. The

maximum runout distance considered is the maximum end locations measured from the foot of the slope. To illustrate this point, an example of Quarry 1 is shown below where the wedge formed by JS3 & JS4 was analyzed in RocFall and the possible fall paths are shown in Figure 54 with their corresponding number of blocks that may follow these paths (Figure 55). In this case, a maximum runout distance of 8.2 m is considered with a corresponding angle of reach of 63°.

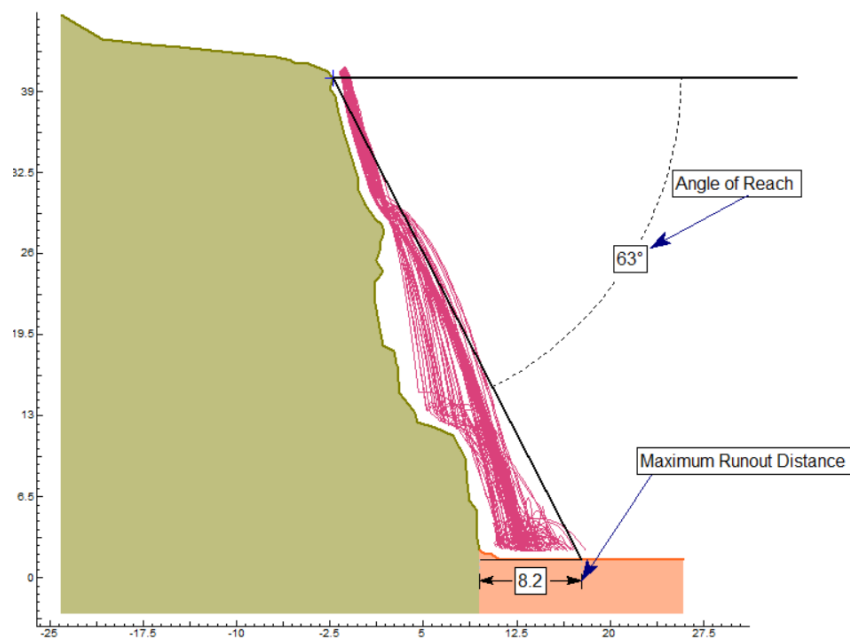


Figure 54: RocFall analysis of the wedge formed by JS3 & JS4 for Quarry 1.

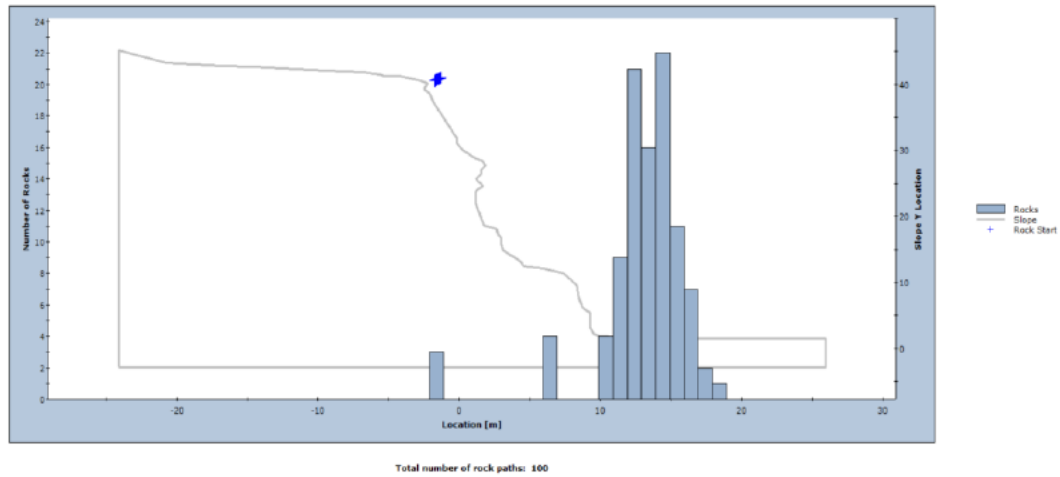


Figure 55: Distribution of rock fall path end locations of the wedge formed by JS3 & JS4 for Quarry 1.

The results are tabulated in Table 12 where the maximum runout distance for each quarry site is highlighted in black.

Table 12: Runout Distance and Angle of Reach calculated using RocFall

| Location | Joint Set Intersections/Joint Set | Weight (MN) | Runout distance (m) | Angle of Reach (°) |
|--------------------|-----------------------------------|-------------|---------------------|--------------------|
| Aarsal | JS4 & JS8 | 2.9 | 6.31 | 65 |
| | JS4 & JS6 | 1.74 | 5 | 68 |
| | JS4 & JS3 | 0.84 | 8.2 | 63 |
| Ain Bourday | JS3 | 5.36 | 7.1 | 65 |
| | JS1 & JS4 | 5.39 | 7.2 | 64 |
| | JS1 & JS9 | 4.23 | 6.4 | 68 |
| | JS1 & JS6 | 2.45 | 5.9 | 70 |
| | JS1 & JS10 | 3.31 | 6.1 | 62 |
| | JS10 & JS9 | 5.73 | 7.2 | 64 |
| Janta | JS1 & JS10 | 0.2 | 6.34 | 69 |
| | JS8 & JS4 | 0.22 | 6.4 | 68 |
| Raiit | JS4 & JS7 | 0.65 | 8.3 | 67 |
| | JS4 | 5.4 | 9 | 65 |

One limitation of the 2D rockfall simulation is the lack of the lateral trajectory dispersion modeling. Therefore, the hazard associated with rockfalls for each quarry was assumed to be in the area created by offsetting the slope face a distance equal to the maximum runout distance for each site. This was done using QGIS software and the generated hazard map is shown in Figure 56. By examining the landslide hazardous areas of each quarry, it can be seen that the hazard is limited to the quarry site only and any potential rock fall threatens the quarry workers and equipment since the exposure appears to be low. This can be confirmed by reviewing the landslide discussed earlier in Chapter 2 where a limestone quarry failure occurred in New Zealand and resulted in the death of the quarry owner. The quarry face is very similar to the quarries analyzed in this study as they all have a steep slope with a slope height of 40 to 60 m. Looking at the rock blocks that have fallen (Figure 57), we notice that these blocks have reached a small runout distance (no more than 10 meters).

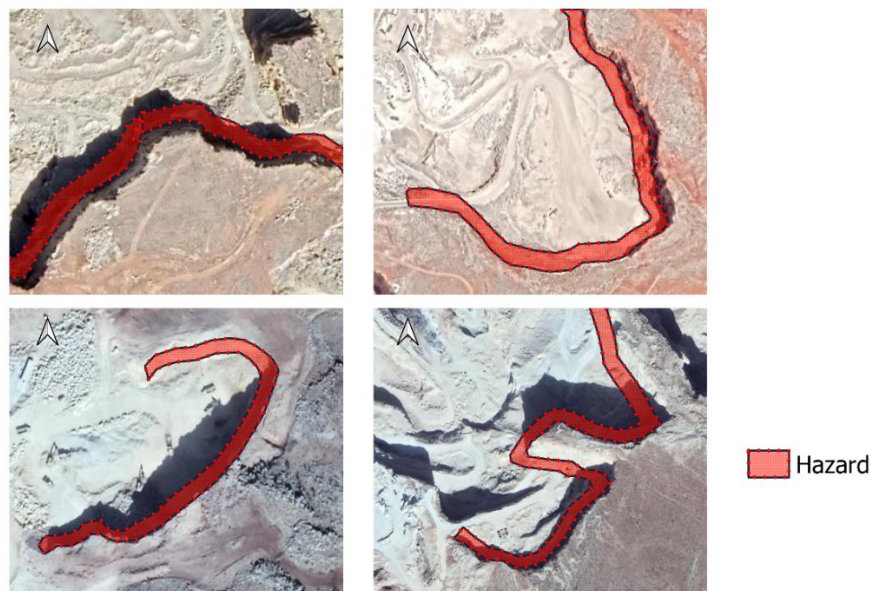


Figure 56: Rockfall Hazard shown in QGIS for a) Quarry 1, b) Quarry 2, c) Quarry 3, and d) Quarry 4



Figure 57: Limestone Quarry Failure in New Zealand

Chapter Five

Conclusion and Limitations

In the present research, remote sensing with UAV provided powerful tool for effectively studying the stability of limestone quarries. This technique was used to construct 3D models of four quarries located in the Anti-Lebanon mountain. The resultant high resolution point clouds were then assessed by extracting geological features used to characterize the rockmass. This included determining the orientation and spatial distribution of discontinuities as well computing the in-situ block size. This data was then used to conduct a kinematic analysis to highlight areas of potential failure with their possible mechanism. The results showed that wedge failure is the most likely failure mode at quarry sites with a probability of 50%. Two of the analysed slopes also showed possible planar failure while none showed any potential toppling failure.

This study evaluated the stability of rock slopes controlled by the geometry and strength of discontinuities using mode-specific software by RocScience to determine the factor of safety based on limit equilibrium methods under dry, rain, and seismic conditions. The overall slope stability was also assessed based on the GSI classification system using Hoek-Brown failure criterion. The quarries showed an elevated risk of block failure that was predicted to occur along discontinuities where shear stress is expected to exceed the shear strength along them. The quarries did not show a risk of general failure. Finally, the maximum runout distance and the corresponding angle of reach were determined. From the four analysed quarries, we can conclude that the maximum runout distance is limited to 9 meters.

The results of this study serve to update the regional scale landslide hazard and risk maps for Lebanon by limiting the risks associated by any potential failures in quarry

sites to 9 meters beyond the quarry face. However, these updates were not implemented in this work due to the following limitations. First, the available DEM is relatively coarse (15-m DEM) as the quarry sites were not properly captured, and therefore a more accurate DEM is needed to extrapolate the results to a regional scale. Second, sandstone quarries were not assessed making this study limited to limestone sites.

Moreover, these findings must be interpreted with caution because the analysed sites are characterized by steep slopes with a height of less than 60 meters and the ground at the toe of the slope is a flat terrain. Any difference from these characteristics may increase or decrease the expected maximum runout distance especially if the toe of the slope is inclined because the blocks falling and hitting the ground may tend to travel a higher distance due to the component of the block weight parallel to the ground (Figure 58) that will act as a driving force.

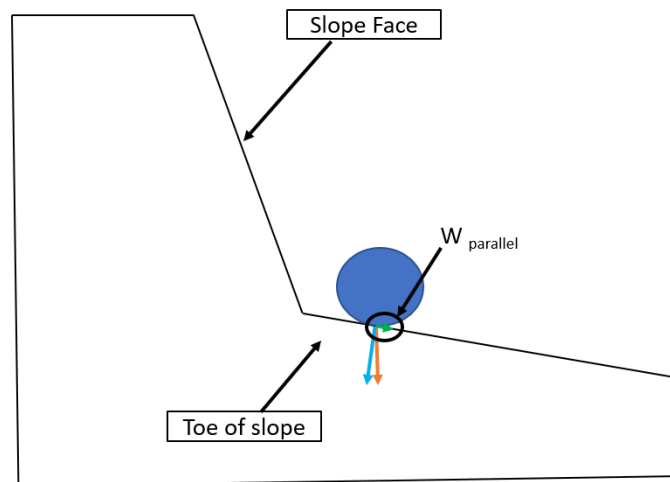


Figure 58: Sketch showing the toe of slope and the parallel component of the weight

Another limitation of this study is the absence of input from a geologist when evaluating the geological features of the quarries. A geologist can provide valuable information about the rock discontinuities and rock strength.

References

- Abdallah, C. (2011). Assessment of erosion, mass movements, and flood risks in Lebanon. In H. Kouyoumjian & M. Ham (Ed.). *Review and Perspectives of Environmental Studies in Lebanon*, 225-246. National Council for Scientific Research (CNRS), Beirut, Lebanon
- Abdullah, R., Yusufianshah, D., Alel, M., Jusoh, S., Hezmi, M., & Yunus, M & Ali, A.N. & Ali., A. (2018). Slope stability analysis of quarry face at Karang Sambung district, central Java, Indonesia. *International Journal of Civil Engineering and Technology*, 9, 857-864.
- American Society for Testing and Materials. (2017). ASTM standard ASTM/ D2938-95: Standard Test Method for Unconfined Compressive Strength of Intact Rock Core Specimens. <https://doi.org/10.1520/D2938-95>
- Anderson, M. G., & Holcombe, E. (2013). *Community-based landslide risk reduction: Managing disasters in small steps*. THE WORLD BANK. <https://doi.org/10.1596/978-0-8213-9456-4>.
- Atallah, Th., Hajj, S., Rizk, H., Cherfane, A., El-Alia, R., Delajudie, P. (2003). Soils of urban, industrial, traffic and mining. *SUITMA*, Nancy, Paris. 9-11
- Azzoni, A., & De Freitas, M. (1995). *Experimentally Gained Parameters, Decisive for Rock Fall Analysis*. *Rock Mechanics and Rock Engineering* 28 (2), 111-124.
- Bar, N., Borgatti, L., Donati, D., Francioni, M., Salvini, R., & Ghirotti, M. (2021). Classification of natural and engineered rock slopes using UAV photogrammetry for assessing stability. *IOP Conference Series. Earth and Environmental Science*, 833(1)<https://doi.org/10.1088/1755-1315/833/1/012046>
- Barton, N.R. & Bandis, S.C. (2017). *Characterization and modelling of the shear strength, stiffness and hydraulic behaviour of rock joints for engineering purposes*. *Rock Mechanics and Engineering*, Ed. Xia-Ting Feng, Vol. 1, Ch. 1, pp. 3-40. Taylor & Francis.
- Basahel, H. & Mitri, H. (2017). Application of rock mass classification systems to rock slope stability assessment: A case study. *Journal of Rock Mechanics and Geotechnical Engineering*, 9(6), 993-1009. <https://doi.org/10.1016/j.jrmge.2017.07.007>
- Bressan, D. (2013). September 11, 1881: The landslide of Elm. *History of Geology*. Retrieved from: <https://blogs.scientificamerican.com/history-of-geology/september-11-1881-the-landslide-of-elm/>
- Chaminé, H. I., Afonso, M. J., Ramos, L., & Pinheiro, R. (2014). Scanline sampling techniques for rock engineering surveys: Insights from intrinsic geologic variability and uncertainty. (pp. 357-361). Springer International Publishing. https://doi.org/10.1007/978-3-319-09060-3_61

- Crozier, M., & Glade, T. (2005). Landslide hazard and risk: Issues, concepts and approach. In T. Glade, M. Anderson & M. J. Crozier (Eds.), (pp. 1-40). John Wiley & Sons, Ltd. <https://doi.org/10.1002/9780470012659.ch1>
- Dadashzadeh, N., Duzgun, H.S.B., Yesiloglu-Gultekin, N., & A. Bilgin. (2014). Comparison of Lumped Mass and Rigid Body Rockfall Simulation Models for the Mardin Castle, Turkey. Paper presented at the 48th U.S. Rock Mechanics/Geomechanics Symposium, Minneapolis, Minnesota.
- Darwish, T. M., Stehouwer, R., Miller, D., Sloan, J., Jomaa, I., Shaban, A., Khater, C., & Hamzé, M. (2008). Assessment of abandoned quarries for revegetation and water harvesting in Lebanon, East Mediterranean. In *25th Annual Meetings of the American Society of Mining and Reclamation and 10th Meeting of IALR 2008* (pp. 271-284). (25th Annual Meetings of the American Society of Mining and Reclamation and 10th Meeting of IALR 2008; Vol. 1).
- Darwish, T., Khater, C., Jomaa, I., Stehouwer, R., Shaban, A., & Hamzé, M. (2011). Environmental impact of quarries on natural resources in Lebanon. *Land Degradation & Development*, 22(3), 345-358. <https://doi.org/10.1002/ldr.1011>
- Dransch, D., Rotzoll, H., & Poser, K. (2010). The contribution of maps to the challenges of risk communication to the public. *International Journal of Digital Earth*, 3(3), 292-311. <https://doi.org/10.1080/17538941003774668>
- El-Fadel, M., Sadek, S., & Chahine, W. (2001). Environmental management of quarries as waste disposal facilities. *Environmental Management (New York)*, 27(4), 515- 531. <https://doi.org/10.1007/s002670010167>.
- Froude, M., & Petley, D. (2018). Global fatal landslide occurrence from 2004 to 2016. *Natural Hazards and Earth System Sciences*, 18(8), 2161- 2181. <https://doi.org/10.5194/nhess-18-2161-2018>
- Goodman, R. E. (1989). *Introduction to rock mechanics* (2nd ed.). Wiley.
- Grant, A., Wartman, J., & Abou-Jaoude, G. (2016). Multimodal method for coseismic landslide hazard assessment. *Engineering Geology*, 212, 146-160. <https://doi.org/10.1016/j.enggeo.2016.08.005>
- Guzzetti, F., Carrara, A., Cardinali, M., Reichenbach, P. (1999). Landslide hazard evaluation: a review of current techniques and their application in a multi-scale study, Central Italy. *Geomorphology*, 31(1-4), 181-216. [https://doi.org/10.1016/S0169-555X\(99\)00078-1](https://doi.org/10.1016/S0169-555X(99)00078-1).
- Hack, H. R. G. K. (1993). Slopes in rock. In *Proceedings: an overview of engineering geology in The Netherlands. - T.U. Delft, 1993, pp. 111-119.* (pp. 111-119). Delft University of Technology.

- Harajli, M., Sadek, S., & Asbahan, R. (2002). Evaluation of the seismic hazard of Lebanon. *Journal of Seismology*, 6(2), 257-277. <https://doi.org/10.1023/A:1015687602473>
- Hoek, E. & Brown, E.T. (1980a). Underground excavations in rock. *London: Institution of Mining and Metallurgy*
- Hoek, E. & Brown, E.T. (1980b). Empirical strength criterion for rock masses. *Journal of the Geotechnical Engineering Division*, 106(GT9):1013e35.
- Hoek, E. & Brown, E.T. (2019). The Hoek–Brown failure criterion and GSI – 2018 edition. *Journal of Rock Mechanics and Geotechnical Engineering*, 11(3), 445-463.
- Hudson, J. A., & Harrison, J. P., (1997). *Engineering rock mechanics: An introduction to the principles* (1st ed.). Elsevier Science & Technology.
- Huijjer, C. & Harajli, M. & Sadek, S. (2011). Upgrading the seismic hazard of Lebanon in light of the recent discovery of the offshore thrust fault system. *Lebanese Science Journal* 12, 67-77.
- Huijjer, C. (2010). Implications of the recent mapping of the offshore thrust fault system on the seismic hazard of Lebanon. (Master's thesis, American University of Beirut, Beirut, Lebanon).
- Huijjer, C., Harajli, M., & Sadek, S. (2011). Upgrading the seismic hazard of Lebanon in light of the recent discovery of the offshore thrust fault system. *Lebanese Science Journal*, 12(2).
- Kaafarani, R. (2020). Landslide Hazard and Risk Level Assessment of Quarried Slopes in Lebanon using Drone Imagery. (Master's thesis, Lebanese American University, Byblos, Lebanon).
- Karakas, A. (2008). Practical Rock Engineering. *Environmental and Engineering Geoscience*, 14(1), 55–57. doi:10.2113/gseegeosci.14.1.55
- Karaman, K., Ercikdi, B., & Kesimal, A. (2013). The assessment of slope stability and rock excavatability in a limestone quarry. *Earth Sciences Research Journal*, 17(2), 169-181.
- Manousakis, J., Zekkos, D., Saroglou, H., Kallimogiannis, V. & Bar, N. (2019). Analysis of slope instabilities in the Corinth Canal using UAV-enabled mapping. *ICONHIC 2019: 2nd International Conference on Natural Hazards & Infrastructure*.
- Matsui, T. & San, K. (1992). Finite Element Slope Stability Analysis by Shear Strength Reduction Technique. *Soils and Foundations*, 32(1): 59-70.
- Memon, Y. (2018). A comparison between limit equilibrium and finite element methods for slope stability analysis.

- MOE, UNDP, & ECODIT (2011). State and Trends of the Lebanese Environment Report.
- Moubayed, S. (2018). Lebanon scrambles to cope with Baalbek floods. *Gulf News*. <https://gulfnews.com/world/mena/lebanon-scrambles-to-cope-with-baalbek-floods-1.2236803>
- Mrad, M., Saad, G., Chehab, G., & Mrad, R. (2017). *Experimental and Statistical Investigation of the Mechanical Properties of Limestone Rocks in Lebanon*. Paper presented at the 10th International Conference on the Bearing Capacity of Roads, Railways and Airfields (BCRRA 2017), June 28-30, 2017, Athens, Greece - ISBN 9781138295957
- Nader, F. (2014). The Geology of Lebanon. Petroleum Geology.
- Pantelidis, L. (2009). Rock slope stability assessment through rock mass classification systems. *International Journal of Rock Mechanics and Mining Sciences (Oxford, England: 1997)*, 46(2), 315-325. <https://doi.org/10.1016/j.ijrmms.2008.06.003>
- Petley, D. (2021). The 31 May 2021 landslide at the Bingham Canyon mine. American Geophysical Union. Retrieved from: <https://blogs.agu.org/landslideblog/2021/06/04/2021-bingham-canyon/>
- Plassard, J. (1971). Rainfall map of Lebanon at scale 1/200,000. Ministry of Public Works. General Directorate of Civil Aviation.
- Pollock, W., Grant, A., Wartman, J., & Abou-Jaoude, G. (2019). Multimodal method for landslide risk analysis. *Methodsx*, 6, 827.
- Prakasam, C., Aravinth, R., Kanwar, V. S., & Nagarajan, B. (2021). Mitigation and management of rainfall induced rockslides along the national highways of himalayan region, india. *Geomatics, Natural Hazards and Risk*, 12(1), 1402-1425. <https://doi.org/10.1080/19475705.2021.1928772>.
- Public Works Studio (2019, April 17). Reading the Quarries' Map in Lebanon. Retrieved from <https://www.jadaliyya.com/Details/38569/Reading-the-Quarries%E2%80%99-Map-in-Lebanon>
- Rahardjo, H., Lim, T., Chang, M.F., & Fredlund, D.G. (1995). Shear-strength characteristics of a residual soil. *Canadian Geotechnical Journal*, 32(1), 60-77. <https://doi.org/10.1139/t95-005>
- Rawat, P., & Sharma, A. (2012). Geo-diversity and its hydrological response in relation to landslide susceptibility in the Himalaya: a GIS-based case study. *Georisk: Assessment and Management of Risk for Engineered Systems and Geohazards*, 6:4, 229-251. <http://doi.org/10.1080/17499518.2012.739701>.

- Riquelme, A. J., Abellán, A., Tomás, R., & Jaboyedoff, M. (2014). A new approach for semi-automatic rock mass joints recognition from 3D point clouds. *Computers & Geosciences*, 68, 38-52. <https://doi.org/10.1016/j.cageo.2014.03.014>
- Riquelme, A., Abellán, A., Tomás, R., Jaboyedoff, M. (2014). Rock slope discontinuity extraction and stability analysis from 3D point clouds: application to an urban rock slope. *Vertical Geology Conference*
- Riquelme, A., Cano, M., Tomás, R., & Abellán, A. (2017). Identification of Rock Slope Discontinuity Sets from Laser Scanner and Photogrammetric Point Clouds: A Comparative Analysis. *Procedia Engineering*, 191. <https://doi.org/10.1016/j.proeng.2017.05.251>.
- Robiati, C., Eyre, M., Vanneschi, C., Francioni, M., Venn, A., & Coggan, J. (2019). Application of remote sensing data for evaluation of rockfall potential within a quarry slope. *ISPRS International Journal of Geo-Information*, 8(9), 367. <https://doi.org/10.3390/ijgi8090367>
- Robotham, M., Wang, H., & Walton, G. (1995). Assessment of risk from rock fall from active and abandoned quarry slopes. Institution of mining and Metallurgy, Section A 104, A25-A33.
- Salvini, R., Francioni, M., Riccucci, S., Bonciani, F., & Callegari, I. (2013). Photogrammetry and laser scanning for analyzing slope stability and rock fall runout along the Domodossola–Iselle railway, the Italian alps. *Geomorphology (Amsterdam, Netherlands)*, 185, 110-122. <https://doi.org/10.1016/j.geomorph.2012.12.020>
- Singh, P. K., Kainthola, A., Panthee, S., & Singh, T. N. (2016). Rockfall analysis along transportation corridors in high hill slopes. *Environmental Earth Sciences*, 75(5), 1-11. <https://doi.org/10.1007/s12665-016-5489-5>.
- Sivakugan, N., Das, Braja M. & Shukla, S. K. (2013). *Rock mechanics: an introduction*. Boca Raton, FL: CRC Press
- Suri, S., Juhari, A., Yaacob, S., Anua, N., Zabidi, H. (2020). Rock slope discontinuity extraction from 3D point clouds: Application to an open pit limestone quarry. *Warta Geologi*, Vol. 46. <https://doi.org/10.7186/wg462202011>
- Wang, S., Zhang, Z., Wang, C., Zhu, C., & Ren, Y. (2019). Multistep rocky slope stability analysis based on unmanned aerial vehicle photogrammetry. *Environmental Earth Sciences*, 78(8), 1-16. <https://doi.org/10.1007/s12665-019-8145-z>
- Wyllie, D. C. (2015). *Rock fall engineering*. CRC Press.
- Zhang, L. (2017). *Engineering Properties of Rocks* (2nd ed). Butterworth-Heinemann.